**Consiglio Nazionale
delle Ricerche**

CNR ISAC

Tecnologie e modelli a supporto delle Scienze dell'Atmosfera e del Clima

Curatori:

Elisabetta Masetti

Maria Cristina Facchini

AUTORI:

Maurizio Busetto

Leopoldo Fazioli, Fabio Massimo Grasso, Antonio Olita

SOMMARIO

Progettazione di un sistema di campionamento nebbie

Maurizio Busetto
ISAC-CNR

1. Descrizione sistema di campionamento

Il campionatore di nebbie ISAC è composto da:
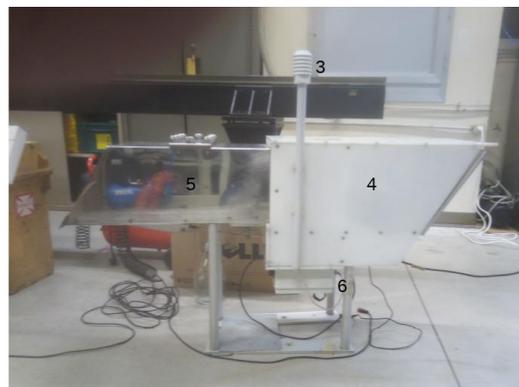
1- PVM-100; 2- Calibratore PVM; 3- T/RH; 4- Ventola; 5- Griglia; 6- Elettronica

L'elettronica di controllo provvede ad avviare la ventola creando il flusso per necessario a campionare la nebbia quando il valore di LWCf fornito dal PVM-100 è superiore ad una soglia fornita dall'utente (tipicamente 0.08 gm^3) e la T esterna non è inferiore ad una soglia definibile, normalmente di poco superiore a 0 gradi centigradi per evitare ghiacciamento delle gocce d'acqua.

Quando il valore di PVM-100 torna inferiore al limite impostato, oppure la temperatura diventa inferiore alla soglia di temperatura, la ventola viene fermata ed il campionamento è sospeso.

Ogni apertura della ventola corrisponde all'inizio di un evento di campionamento che dura fino allo spegnimento della ventola. Una bottiglia può contenere più eventi, qualora all'interno della stessa bottiglia sia superato un numero massimo di eventi possibili, definibile dall'utente, la ventola non verrà attivata onde evitare tracimazione dell'acqua dalla bottiglia di campionamento.

Per evitare chiusure-aperture repentine non dovute a nebbie importanti, oppure dovute ad interferenze (tipica è la formazione di ragnatele vicino all'ottica del PVM-100), il valore di LWCf e di T

da utilizzarsi come soglia per il comando della ventola sono calcolate come media trascinata su un numero di minuti definibile delle medie al minuto ottenute con una frequenza di misura di un secondo.

L'elettronica di controllo è inoltre dotata di telecamera che scatta una fotografia della bottiglia ogni ora, tale telecamera può essere inoltre attivata per scattare foto a richiesta da comando remoto. L'opzione telecamera permette di vedere da remoto lo stato della bottiglia in modo da poter decidere quando è necessario recarsi sul posto per cambiare la bottiglia.

I dati e le fotografie vengono inviati ad un server ISAC (*ferrarese.bo.isac.cnr.it)* e visualizzati in apposita pagina web.

Collegamenti campionatore

L'elettronica di controllo del campionatore presenta appositi connettori per il collegamento con i vari appartai del sistema e dei tasti per alcuni controlli, che vengono illustrati nelle figure seguenti

Figura 1: sistema di campionamento

Il connettore 1 serve per ricevere i segnali dal PVM-10 in modo da avere la misura di LWCf, il connettore 2 serve per portare il segnale di accensione e spegnimento alla ventola.
Il pulsante per cambio bottiglia si preme quando si effettua l'operazione di sostituzione della bottiglia e serve per l'identificazione con numeri consecutivi della bottiglia in relazione agli eventi di nebbia campionati. Il numero della bottiglia viene salvato sul file di dati.
La porta ethernet serve sia per collegarsi in caso di mancanza di rete wifi che per settare la wifi all'installazione in campo del sistema di campionamento.

Formato dati e visualizzazione su web server

I dati vengono salvati in un'apposita SD dell'elettronica ed inviati tramite TCP/IP ad un server ISAC (*ferrarese.bo.isac.cnr.it*). I file di dati sono a livello giornaliero:

Nome file: *Nebbie_SPC_yyyymmdd.dat*

header:

- *date*: data nel formato yyy-mm-dd
- *time*: ora nel formato HH:MM:00 (arrotondamento al minuto più prossimo)
- *daydec*: giorno decimale calcolato usando 0 come 1° gennaio
- *T*: media al minuto T misurata ogni secondo
- *RH*: media al minuto RH misurata ogni secondo
- *PVM*: media al minuto LWCf misurata dal PVM-100 ogni secondo
- *bottle*: numero di bottiglia campionata
- *event*: numero di evento per bottiglia, se 0 non in campionamento
- *force*: indica se il campionatore è in funzionamento normale 0, in apertura forzata 1
    o in chiusura forzata (-1)
- *T_ave*: media trascinata su N minuti di T
- *PVM_ave*: media trascinata su N minuti dei valori di LWCf

Viene inoltre creato il file *Nebbie_eventi.dat* che riassume i parametri di ogni singolo evento della campagna di misura, tale file ha il seguente header

- *bottle.event*: numero bottiglia.numero evento
- *start_date*: data e ora di inizio evento
- *stop_date*: data e ora di fine evento
- *duration[min]*: durata in minuti dell'evento
- *T_ave*: T media registrata durante l'evento
- *PVM_ave*: LWCf medio registrato durante l'evento

La pagina web dove viene visualizzato il funzionamento del campionatore (h*ttp://ferrarese.bo.isac.cnr.it/FogSampler.html) riporta* informazioni:

- grafici delle ultime 24 di LWCf T e RH con evidenziati in colore blu i periodi di campionamento
- ultimi dati acquisiti dal campionatore (ultima riga ultimo file dati presente sul server)
- dati relativi all'ultimo evento di nebbia campionato (ultima riga file Nebbie_eventi.dat)
- le immagini della bottiglia all'inizio ed alla fine dell'ultimo evento e l'ultima foto scattata da remoto

Nella pagina seguente viene riprodotta una pagina web come esempio
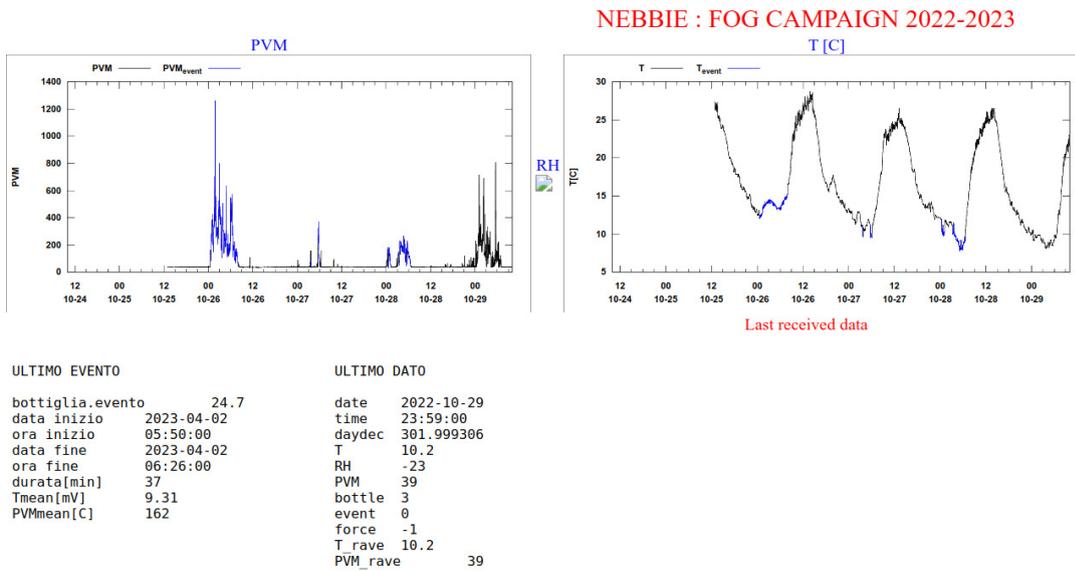
figura 2: pagina web del sistema del campionamento

Sostituzione bottiglia

Quando dall'immagine sulla pagina web si vede che la bottiglia è piena si deve procedere alla sua sostituzione nel seguente modo:

- svitare il tappo della bottiglia ed il blocco sul campionatore (manopola laterale)
- pulire le tre griglie con acqua distillata
- mettere la nuova bottiglia assicurandosi di aver ben avvitato tappo e blocco sul campionatore
- premere il pulsante di cambio bottiglia

2. Utilizzo del sistema di campionamento

Impostazione rete e collegamento col sever ISAC

Per impostare la wifi collegarsi alla presa ethenet da un PC, settando sul PC un indirizzo 172.16.64.xxx, ed utilizzando i seguenti parametri per la comunicazione ssh tramite putty (windows) o terminale (linux):

host=172.16.64.30; username=pi; password=N&bbie

una volta connessi col campionatore digitare *sudo raspi-config* e selezionare *Network Option.*

quindi impostare la SSID e la password della rete wifi a cui ci si collega.

Dopo il reboot il campionatore attiva la VPN col server *ferrarese*, una volta attiva la VPN il campionatore diventa raggiungibile da remoto tramite il server ed invia ad esso i dati della misura.

Per raggiungere il campionatore dal server ferrarese digitare *connect_nebbie* sul terminale del server.

Nota, se si vuole integrare il campionatore in una rete ethernet, bisogna cambiare l'indirizzo fisso impostato sulla eth0 del raspberry agendo sul file etc/dhcpcd.conf

Menu di utilizzo

Per poter fornire dei comandi al campionatore bisogna accedere al menu (tramite VPN, wifi o ethernet) e digitare *menu* sul terminale dello strumento.

Nella schermata principale del menu (figura 1) viene riportato se il programma di acquisizione è in esecuzione o meno, gli ultimi dati registrati e le opzioni di controllo del campionatore.
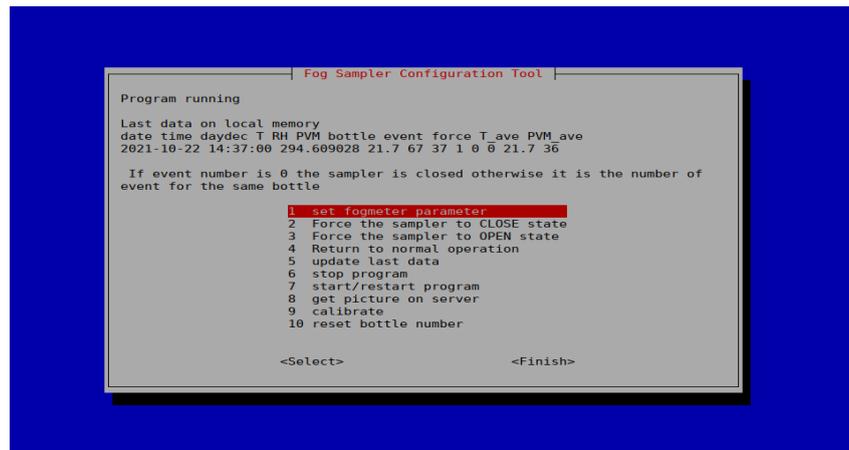
Figura 3: schermata principale del menu

Per muoversi sul menu usare i tasti freccia, per selezionare <select> o <finish> usare il tasto tab.

L'opzione 1 (set fogmeter parameters), come riportato in figura 4, visualizza i seguenti parametri di funzionamento del campionatore:

station: nome del luogo dove viene installato il campionatore

maxevent: campionamenti massimi permessi per singola bottiglia

ravestep: numero di minuti sui quali viene calcolata la media trascinata di T e PVM da confrontarsi con i valori soglia

tsoglia: valore di temperatura al di sotto del quale il campionamento è interdetto

pvmsoglia: valore di oltre il quale si attiva il campionamento
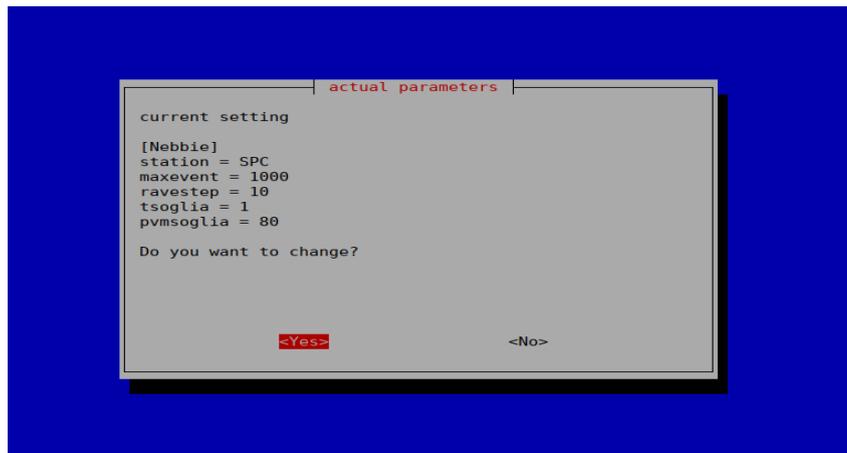
Figura 4: visualizzazione parametri di funzionamenti

scegliendo YES si accede alla finestra, visualizzata in figura 5, che permette di scegliere quale parametro cambiare (figura 5)
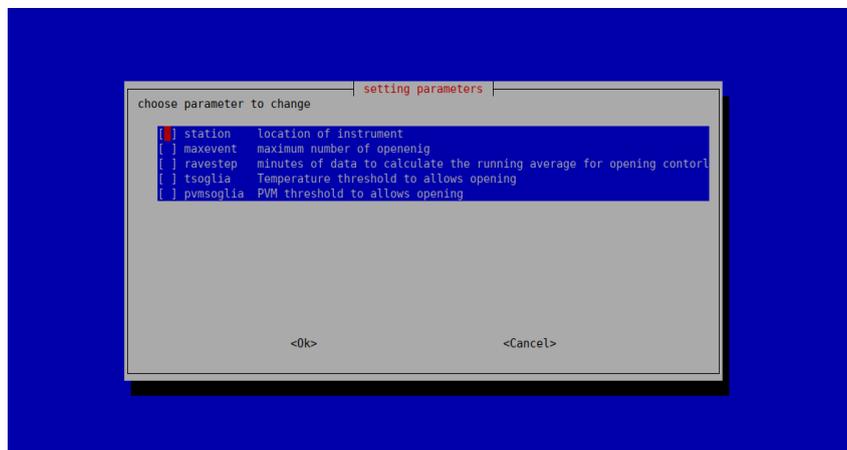
Figura 5: scelta parametri da configurare

scorrendo il menu con i tasti freccia, scegliendo il parametro con il tasto spazio e dando OK si accede alla schermata che permette di cambiare il parametro scelto, come riportato in figura 6 per il parametro Tsoglia:
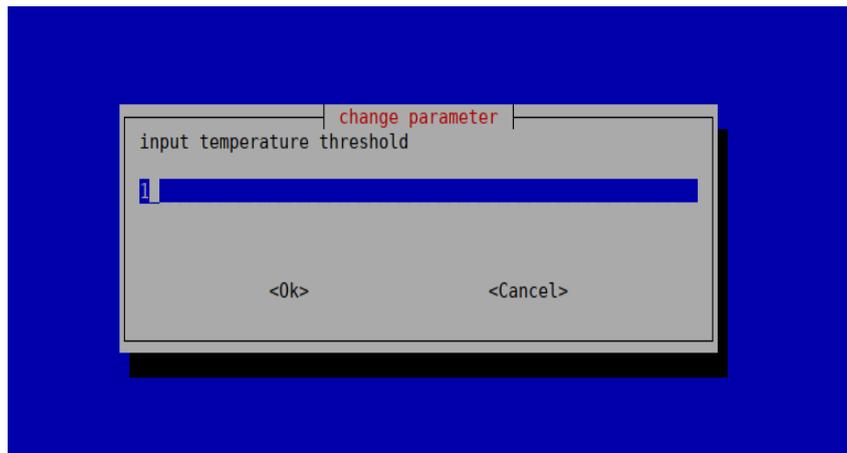
Figura 6: settaggio del parametro

inserendo il nuovo valore e dando OK il parametro viene cambiato.

L'opzione 2 (Force the sampler to CLOSE state) serve per forzare il campionatore a non campionare anche se le condizioni sono favorevoli.

L'opzione 3 (Force the sampler to OPEN state) serve per forzare il campionatore a campionare anche se le condizioni non sono favorevoli.

L'opzione 4 (return to normal operation) serve per ritornare al normale funzionamento del campionatore dopo aver scelto l'opzione 2 o l'opzione 3.

L'opzione 5 (update last data) serve per fare un refresh degli ultimi dati nella schermata principale del menu (Figura 1).

L'opzione 6 (stop program) serve per fermare il software del campionatore, di fatto rendendolo non operativo.

L'opzione 7 (start/restart progarm) serve per avviare o riavviare il software del campionatore, di fatto rendendolo operativo

L'opzione 8 (get picture on server) serve per scattare una fotografia alla bottiglia di campionamento, tale fotografia verrà inviata al server ferrarese e visualizzata nella pagina web dedicata alla campagna delle nebbie *http://ferrarese.bo.isac.cnr.it/NEBBIE.html*

L'opzione 9 (calibrate) serve per effettuare la calibrazione del PVM.

Scegliendo tale opzione sul terminale appariranno i valori letti dal PVM ogni secondo per un minuto di tempo.

Per effettuare la calibrazione mettere il vetro opaco sul calibratore dal lato dove è scritto *cal* con la freccia rivolta verso la sorgente laser il valore atteso è 95. Agire sul trimmer del PVM fino a quando sul terminale non compare il valore 95

Durante la calibrazione il software del campionatore viene fermato, pertanto per effettuare i campionamenti bisogna scegliere opzione *6-Start/restart program* in quanto durante la calibrazione il sistema non è in acquisizione.

L'opzione 10 (reset bottle number) serve a resettare il numero della bottiglia portandolo ad 1. È obbligatorio lanciarlo all'inizio della campagna di misura.

3. ALLEGATO 1: Schema elettronica di controllo

ALLEGATO 2: schema sistema di ventole
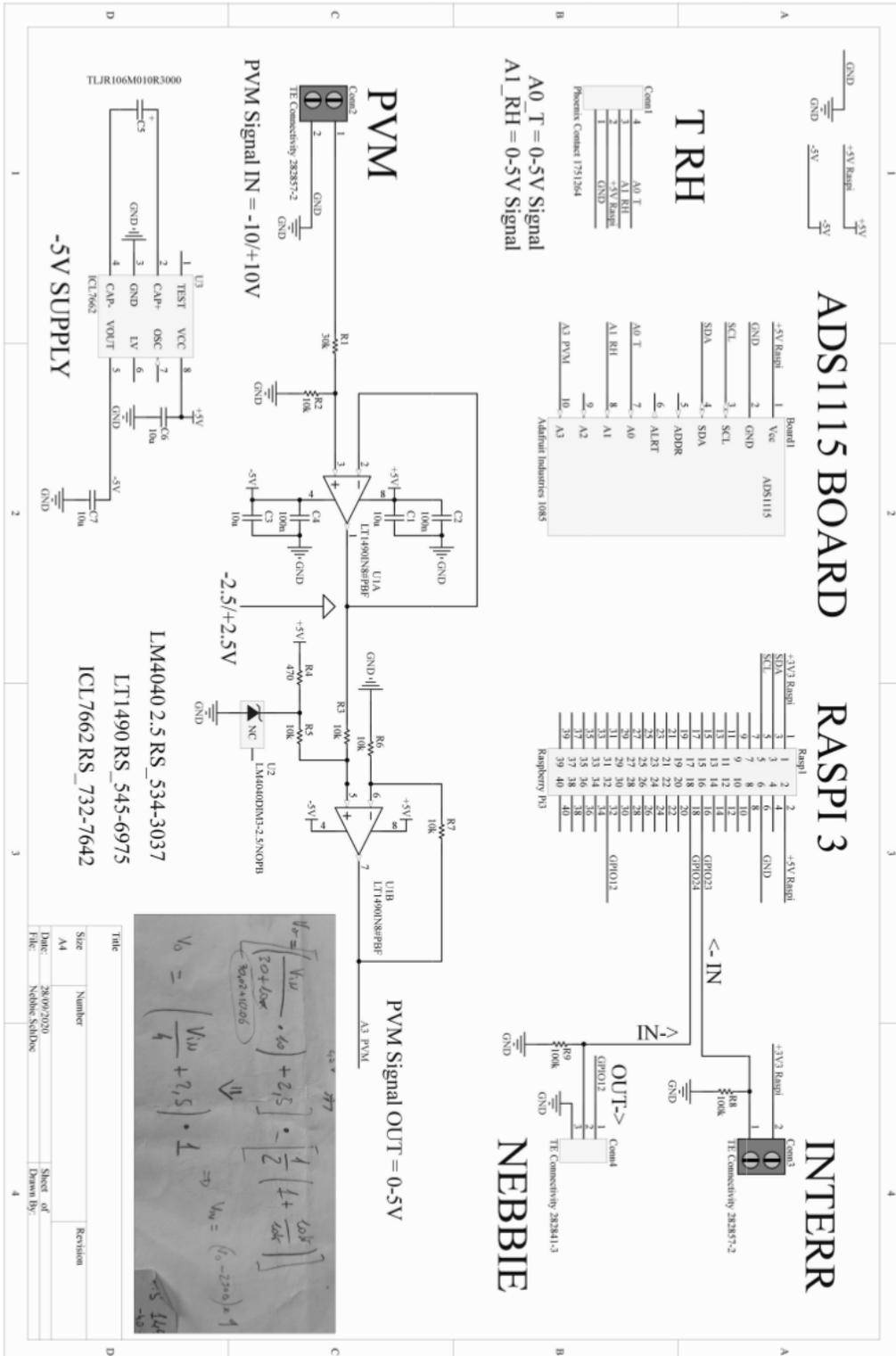
Forecasting surface winds and temperatures over complex topography: the Sardinia island case study

Leopoldo Fazioli, Fabio Massimo Grasso, Antonio Olita
ISAC-CNR

1. Introduction

Near surface forecasting of atmospheric conditions is an extremely complex matter [e.g. 1] due to the uniqueness of the bottom of the atmospheric boundary layer i.e. the part of the bottom atmosphere physically interacting with the Earth surface. Peculiar processes of this particular layer include a strong diurnal variation of temperatures and turbulence caused by topography, who forces wind field to behave differently from the upper layers. The uniqueness also stands in the fact that here (in the bottom of lower atmosphere) a large part of the planet's life (and by the way the whole humanity) spends its existence. One of the big challenges for the humankind is the sustainability of the population that is currently increasing of about 1 % per year. Sustainability it means basically that population growth must be in the limit of the resources exploitation. Nowadays the primary resource for human populations sustainability is energy. The energy supply, to limit consequences of anthropogenic climate change and to maintain and even increase sustainability of the human populations on earth, has to be moved from fossil fuels to renewable energies, primarily solar and wind energy. Optimization of wind energy exploitation in turn goes through an optimization of the location and usage of turbines (the current main technology on which is based the wind energy supply). In order to optimize wind farms efficiency, a skilled weather forecasting model able to predict at best wind intensity and direction need to be set up [e.g. 2], at a resolution suitable to describe enough in details the underneath topography, and with a locally optimized parameterization for the Planetary Boundary Layer [PBL hereafter, e.g. 3, 4]. Bottom Boundary layer (i.e. first bottom meters) temperatures are also one of the main meteorological parameters, together with winds and daily precipitations, of interest for the users accessing (through web portals for instance) weather forecasts. These two parameters, surface temperatures and winds (both intensities

and directions), are highly variable in short space scales over complex topography, and constitute a big challenge in current high-resolution weather forecasting and nowcasting services [1]. For the present work we adopted the Weather Regional Forecasting model 2 [WRF, 5] with two different setups, to evaluate the skill of the model to forecast bottom boundary layer winds and temperatures during a 11-days quasi-stable period, with an incursion of some instability at the end (last 3 days) of the 11-days period. Thus, WRF is the atmospheric model at the core of the local implementation that we named MoSarT (Models of Sardinia Toolkit). This system, in our vision, will become a state-of-the-art toolkit that will be able to simulate the regional earth system of the Sardinia and surrounding area and that will encompass, in the near future, the implementation of different coupled modeling tools for different earth system compartments (e.g. atmospheric aerosol and chemistry, air-sea interactions, ocean circulation, etc). The system should also encompass an open source observation network for online and offline validation and for Data Assimilation. For the present work, a network of 97 weather stations, providing 2 m temperatures and 10 m wind intensity and direction, has been used to evaluate the ability of the model to foresee the behavior of such parameters close to the land surface. The report is organized as follows: section 2 describe the area and the synoptic circulation for the study location and period; section 3 speaks about data, the model and analyses methods are described; section 4 shows the results comparing the two implementations; finally, section 5 draws conclusions and depicts possible future developments for the MoSarT system.

2. Study Area and synoptic description

We focused our attention to Sardinia, the second larger island of the Mediterranean with an extension over the 24000 square kilometers. The territory is topographically complex, with a single and elongated flat-land disposed NW-SE included in a substantially heterogeneous rocky mountain landscape. Topography is complex, with deep and narrow canyons, valleys, some mountain higher than 1500 m and cliffs in many stretches of the coastline but especially along the eastern coast of the Island, where they can exceed 300 meters. As a test 3 case we chosen a 11-days period (Sept. 24, 2019 to Oct. 3, 2019). For this particular period of relatively calm

winds, we had at disposal a set of data collected by a network of weather stations catalogued and pre-processed by the no-profit organization Sardegna Clima onlus. As evident by observing synoptic maps of Fig.1, at the beginning of the studied period the whole Western Mediterranean Sea and in particular the Sardinia area was characterized by stable weather conditions, testified by the 1019 hPa isobar at sea level over the Sardinia region for the first two days. Such moderate high pressure extends throughout central Europe, varying between 1022 hPa in north Africa and 1026 hPa on the Scandinavian peninsula. At these baric conditions the 2 m temperatures range between 22 and 24 C∘, while 10 m winds range within breeze values. The stable conditions of the first period (lasting for about 7 of 11 days) are confirmed by the geopotential height of 500 hPa which remains stably around 5100m crossing linearly the central Mediterranean. Geopotential heights at 500 hPa begin to drop in the final part of the period under consideration, lowering to about 4900 m accompanied by a 1005 hPa of minimum pressure at sea level. A minimum pressure is located in the northern Tyrrhenian, attracting counterclockwise wind circulation around Sardinia and inducing a general worsening of weather conditions on the Italian peninsula. The 2 m air temperatures on average decrease about 2 C∘ in the central Mediterranean area and up to 3 C∘ on the west coast of Sardinia due to the north western winds blowing up to 25kn, triggered by the baric conditions as described above in Fig.1.

3. Methods and data

Model and experimental setup

MoSarT implementation used for this study is based on Weather Research Forecasting Model (WRF V4.0.3, released on December 18, 2018), a limited-area meteorological model widely diffused in the atmospheric sciences community [6] [5]. In its present form, it consists of three two-ways nested domains, named D1, D2 and D3, with a Lambert conformal projection and regular grid sizes respectively of 9, 3 and 1km. The domains are built by WRF pre-processing System (WPS), using an high resolution 3 sec topography. Each nested domain is entirely embedded in the lower resolution one, as shown in Fig.2. Initial and boundaries

condition were obtained from hourly $0.25\circ$ NCEP (National Center for Environmental Prediction) Global Forecasting System (GFS). We maintained the recommended $1:3$ grid ratio. The number of vertical levels for each domain is 37 while the PBL (Planetary Boundary Layer) scheme chosen is the Yonsei University (YSU) [7] [8], a first-order non local scheme widely used in atmospheric simulations to capture the vertical structure of meteorological and chemical variables. Unified Noah land-surface option is chosen to modeling land surface processes in numerical weather prediction [9]. Longwave and shortwave radiations are calculated using Rapid Radiative Transfer Model (RRTM) [10] and the Dudhia algorithm [11] respectively. Microphysic chosen for all domains is a WRF Single-Moment 6-class(WSM-6class) scheme [12]. The Kain-Fritsch scheme of cumulus is adopted only for the coarser domain [13], while the both inner domains itself solved explicity the cumuls cloud without any parametrisation [14] [15].

Observations and Data processing

In order to evaluate model performances in reproducing winds and 2m air temperatures, we used a set of data derived by the observational network of the Sardegna Clima Onlus no-profit association. The association owns and/or indirectly maintain about 100 weather stations all over Sardinia. The weather 5 stations, of various type and level but ranging from semi-professional to professional in all cases, collect, at different time sampling ranging from few seconds to 5 minutes at most, 2 m temperature and 10 m wind intensity and directions, relative humidity, atmospheric pressure and daily rain. For the present study we focus our attention to 10 m wind and 2 m temperatures. Winds are considered both in term of magnitude and direction. In order to compare observations with hourly model outputs, the observational values are linearly interpolated in time to the model output time vector. For winds, considering the problem of interpolating angles, we converted angular direction and magnitude of winds to U and V components, then we proceeded with the interpolation separately for U and V components; we re-converted obtained U and V data to module (magnitude) and angular direction. For what concern the co-location of stations with simulated values, we opted for the closest grid point to the actual position of the weather station, instead of averaging or interpolating values. This because we were interested to the impact of the resolution

(combined with an improved topography described above). Such an impact, potentially quite small in percentage, can be totally hidden by various interpolation procedures, the reason why we limited them as much as possible.

Metrics

RMSE and BIAS, computed separately over space and time to respectively obtain time series and maps, have been computed for both the experiments between model outputs and observations. For this particular purpose, we took into account the 79 on 97 stations at disposal, since they were included in the area covered by the D3 domain. This because we were interested to observe the effect, on D2 model, of the two-way coupling and the improvement eventually induced by the nesting of the high resolution model (D3, indeed). RMSE is the root mean square error between model and observation, while the BIAS is the Mean difference between the two. The latter represent the systematic error performed by the model in estimating a given physical quantity. Formulas are really not needed, as they are quite common metrics used in geophysics and can be retrieved everywhere. It is worthy to be noticed that the BIAS is positive (negative) for model overestimation (underestimation). RMSE and BIAS have been computed for temperature, wind magnitude (module) and for wind directions. In the particular case of the directions, one should take account of the circular nature of the directions, so the stats have been computed by using a "Circular Statistics toolbox" designed for Matlab R©environment, and freely available there: https://it.mathworks.com/matlabcentral/fileexchange/10676-circular-statistics-toolbox-directional- statistics . Correlations and observational standard deviations have been also computed, daily based, in order to draw the so called [Taylor Diagrams [16] that are able to summarize different metrics of a model skill for a given variable in a single plot.

4. Results

We remind here that the aim of the report is to investigate the improvement in surface wind and temperature forecasting given by the presence of a high (1 km) resolution model capable

to better resolve complex topography, in respect to a moderate (3 km) and coarse (9 km) model solution. We noticed that sometimes the results of the impact of the highest resolution model was clearly visible in the moderate resolution domain, when it receives the feedback from the high-resolution model. So, in some cases, we found not necessary to show all the 4 model solutions (D1, D2nest, D2stand and D3), while a comparison of D2nest and D2stand was sufficient.

Topographic improvement

In order to fully exploit the possibility to improve the model through an increase in resolution, we thought that a first necessary step was the improvement of the topography. In facts, the standard USGS topography provided together with the current WRF release was the 30 sec USGS topography. This it means about 1 km of resolution. This is comparable to the resolution of the finer domain we set up. So, considering that is highly advisable that the original resolution of the topography would be higher than the model resolution, we downloaded and processed a high-resolution topography provided by SRTM (SHuttle Radar Topography Mission) program. This topography is provided at 3s of resolution, so containing information about the model sub-grid variability. Then, once interpolated on model grid, we again obtain a resolution of 1 km, by the way. Nevertheless, we may notice relevant differences in matching the stations location (related to the representation problem) in terms of differences of quota (m) between real and "virtual" stations. In Fig.3 we show the difference between absolute errors for high resolution and low resolution topography, both interpolated to the D3 grid resolution (1 km) in representing the quota of the weather stations considered for validation. Red means that the representation is improved, blue that is worse. On average the absolute error improves of about 11 m. The RMSE of the two quota series is about 47.5 m for high resolution topography and about 60 m for the low resolution, i.e. the RMSE improves of about 12.5 m.

Model skill assessment

The ability to reproduce observed features over the 11 days is synthesized through Taylor Diagrams, already described in methods section and shown in Figs.4 to Figs.7. D1 and D3 clearly show strongly different skills both in winds and temperatures. This was expected as the D1 domain at 9 km is not able to approximate sufficiently the actual topography, that impacts on both temperatures and winds. Taylor diagrams clearly show that D2nest and D2stand are almost equal in terms of wind intensities while a difference is shown in terms of RMSD (Root Mean Square Difference) for 2 m temperatures. In particular, for the D2nest implementations RMSD of surface temperatures does not exceed 2 C∘ for the first 7 days, when stable conditions where encountered, while it reaches 2.5 C∘ during the weak perturbation crossing the domain during the first days of October. On the contrary for the uncoupled D2stand setup, RMSD exceeds for about half of the period 3 C∘ of RMSE. Standard deviation is larger for the coupled case and lower for the uncoupled (this probably because the D3 nested domain acts also as smoother of the D2 solution), while the correlation is similar for the two implementations. D1 behavior is largely worse than other model solutions. About wind directions, we noticed strong changes above all depending by the sector the winds blow: lower error is related to westerly (both NW and SW) winds, while larger error is related to easterly winds (NE and SE). This is related probably to the topography (steeper on the Eastern side of the Island and smoother on the western side) but also to the statistical power of the dataset we used. In facts, easterly winds have been largely less frequent than the westerly in the 11 days of the experiment (please see Fig.8 for a synthesis of wind directions in such 11 days). Panels of Fig.9 and 10 clearly depicts this different skill of the model depending by the sector. In this case, just the D2nest and D1 results are presented, as there are not large differences between D2nest, D3 and D2stand solutions, while once again D1 is largely worse than other model solutions. Statistics related to these four sectors are presented in table 1, where are shown values for D1, D2nest, D2stand and D3.

Experiment	NW	SW	NE	SE
D1	37.8∘	56.8∘	101.2∘	90.0∘
D2nest	28.4∘	39.1∘	100∘	76.7∘
D2stand	27.0∘	40.3∘	96.2∘	82.8∘
D3	31.8∘	38.2∘	71.6∘	86.5∘

The table 1 clearly shows the difference in the ability of reproducing directions (only directions of winds stronger than 5 m/s are considered) between westerly and easterly winds, above cited. Differences are also clear among the different resolution, especially it is clear that the D1 model, at 9 km of resolution and thus with an underlying smoothed topography, is not sufficient to properly resolve wind directions. On the other side, there are no big differences by comparing the two D2 implementations, D2nest and D2stand, from the point of view of the wind directions. The differences can be observed in the table are of opposite sign depending by the sectors. Statistics performed directly on the D3 implementation shows a further worsening of such statistics, suggesting that for the 3 on 4 sectors we have no advantages in an increase of resolution in the simulation of the wind directions.

5. Summary and Conclusions

In this work a 2-way nested multiple domain model, named MoSarT and based on WRF, for weather forecasting over the Sardinia region (Western Mediterranean), running in forecast mode (slave mode, [e.g. 17]), is evaluated against a set of in situ observations. Evaluation, over a period of 11 days, is done against observations of 2 m air temperatures and 10 m winds, provided by a network of weather stations owned by SardegnaClimaOnlus. D1, D2 (D2stand and D2nest) and D3, at 9, 3 and 1 km of resolution respectively, are evaluated mainly through basic statistics on wind intensities and air temperatures, synthesized in form of Taylor diagrams [16] able to represent Correlation coefficient, RMSE and Standard deviation in a single plot. D2 implementation was considered with and without (D2nest and D2stand, respectively) the 2 way nesting with D3, that can provide a feedback on the D2 domain by smoothing and correcting

the D2 solution. D2 and D3 topography has been improved through the use of the SRTM high resolution dataset, showing some effect in reducing the so called representation error by about ten meters a.s.l. Results show that D1 (9 km) domain is poorly able to reproduce both winds and temperatures. It is noticeable that D2nest and D3 almost show the same results in terms of air temperature skill, and they behave better than D2 uncoupled solution. This, probably, relates to an improvement of the representation error (the model is more precise in matching the weather station location and elevation) more than an improvement on dynamics due to the increase of the resolution. D2stand shows slightly worse skill in representing temperatures. About winds, once again D1 is not able to simulate accurately local winds, while D2stand, D2nest and D3 provide comparable solutions, in terms of error, both in intensities and directions (cfr. Table 1), confirming the idea that the improvement seen in temperatures is more due to a better matching of the stations than to the development of a different dynamic.

The other rising point, coming from the wind directions validation, is that for all the model implementations the simulated easterly winds have an associated error at least twice the error of winds from westerly sectors. The lowest error is associated to NW sector, that is also largely the most present ventilation in terms of frequency over the whole 11days period. This difference in winds simulation skill could be due once again to the topography of the Island, having its tallest mountains on central/northern area, flat lands on the NW-SE direction and steeper cliffs on the Eastern coast in respect to the milder shapes of the western one, but for sure is also related to the different frequency and strength of the winds blowing by the 4 sectors in the 11-days period.

Our main conclusions are that 9km implementation is largely not sufficient to correctly resolve features in Sardinia region in order to simulate surface dynamics. This has to be kept in mind when using/applying atmospheric models in this area at a resolution comparable to D1 mode (9 km); still, the 3 km and 1 km implementations provide similar solution with an improvement on the surface temperatures for the highest resolution model that could be due to an improvement of the so called representation error (i.e. the error linked to the mismatching between the simulated point with the real observational point) more than to a development of finer dynamics. This considering that winds do not show such difference among

D2nest, D2stand and D3. The 1 km implementation of MoSarT do not showed large improvement in winds intensities and directions in respect to the D2 implementation, while both behave definitely better than D1 at 9 km of resolution. The similarity of D2(stand and nest) and D3, in terms of winds skill, could be related to several factors, among which a limitation on the dataset used, that is provided (concerning directions) discretized in angles of 11.25◦ and not as a continuous distribution. Further, short-term forecast also does not allow the D3 model to develop its own dynamics and to diverge the solution by D2. So, experiments should be done also to evaluate the difference in mid-term forecasts (3-4 days) between D3 and D2 (both coupled and uncoupled) solutions, if any. As future developments of the present work, we will evaluate the possibility of local implementations of a D4 domain at a 300 m of resolution, for instance for wind field modeling in areas of wind farms. Other possible developments will concern vertical levels of the model, increasing their density at the bottom of the lower atmosphere, in order to estimate low winds in presence of high cliffs, probably one of the reason why the NE and SE winds have been poorly estimated by all model solutions.

6. References

[1] H. Zhang, Z. Pu, X. Zhang, Examination of errors in near-surface temperature and wind from wrf numerical simulations in regions of complex terrain, Weather and Forecasting. doi:10.1175/WAF-D-12-00109.1.

[2] M. Giannakopoulou, R. Nhili, Wrf model methodology for offshore wind energy applications, Advances in Meteorology 2014. doi:10.1155/2014/319819.

[3] M. Garcia-Diez, J. Fernandez, Fita, C. Yag¨ue, Seasonal dependence of wrf model biases and sensitivity to pbl schemes over europe, Quarterly Journal of the Royal Meteorological Society 139 (2013) 501–514. doi:10.1002/qj.1976.

[4] E. Avolio, F. Stefano, M. Miglietta, T. Lo Feudo, C. Calidonna, A. M. Semprevima, Sensitivity analysis of wrf model pbl schemes in simulating

boundary-layer variables in southern italy: An experimental campaign, Atmospheric Research 192 (2017) 58–71. doi:10.1016/j.atmosres.2017.04.003.

[5] W. Skamarock, J. Klemp, J. Dudhia, D. Gill, D. Barker, W. Wang, J. Powers, A description of the advanced research wrf version 2, Tech. rep. (06 2005). doi:10.5065/D68S4MVH. [6] W. C. Skamarock, J. B. Klemp, J. Dudhia, D. O. Gill, D. M. Barker, W. Wang, J. G. Powers, A description of the advanced research wrf version 3. ncar technical note-475+ str.

[7] S.-Y. Hong, A new stable boundary-layer mixing scheme and its impact on the simulated east asian summer monsoon, Quarterly Journal of the Royal Meteorological Society 136 (651) (2010) 1481–1496.

[8] S.-Y. Hong, Y. Noh, J. Dudhia, A new vertical diffusion package with an explicit treatment of entrainment processes, Monthly weather review 134 (9) (2006) 2318–2341. [9] M. Tewari, F. Chen, W. Wang, J. Dudhia, M. LeMone, K. Mitchell, M. Ek, G. Gayno, J. Wegiel, R. Cuenca, Implementation and verification of the unified noah land surface model in the wrf model, in: 20th conference on weather analysis and forecasting/16th conference on numerical weather prediction, Vol. 1115, American Meteorological Society Seattle, WA, 2004, pp. 2165–2170.

[10] E. J. Mlawer, S. J. Taubman, P. D. Brown, M. J. Iacono, S. A. Clough, Radiative transfer for inhomogeneous atmospheres: Rrtm, a validated correlated-k model for the longwave (paper 97jd00237), JOURNAL OF GEOPHYSICAL RESEARCH-ALL SERIES- 102 (1997) 16–663.

[11] J. Dudhia, Numerical study of convection observed during the winter monsoon experiment using a mesoscale two-dimensional model, Journal of the atmospheric sciences 46 (20) (1989) 3077–3107. [12] S.-Y. Hong, J. Dudhia, S.-H. Chen, A revised approach to ice microphysical processes for the bulk parameterization of clouds and precipitation, Monthly weather review 132 (1) (2004) 103–120.

[13] J. S. Kain, The kain–fritsch convective parameterization: an update, Journal of applied meteorology 43 (1) (2004) 170–181.

[14] A. Arakawa, J.-H. Jung, C.-M. Wu, Toward unification of the multiscale modeling of the atmosphere., Atmospheric Chemistry & Physics Discussions 11 (1).

[15] M. L. Weisman, W. C. Skamarock, J. B. Klemp, The resolution dependence of explicitly modeled convective systems, Monthly Weather Review 125 (4) (1997) 527–548.

[16] K. E. Taylor, Summarizing multiple aspects of model performance in a single diagram, Journal of Geophysical Research: Atmospheres 106 (D7) (2001) 7183–7192. arXiv:https://agupubs.onlinelibrary.wiley.com/doi/pdf/10.1029/2000JD900719, doi:10.1029/2000JD900719.
URL https://agupubs.onlinelibrary.wiley.com/doi/abs/10.1029/2000JD900719

[17] L. Fazioli, A. Olita, A. Cucco, C. Tedesco, A. Ribotti, R. Sorgente, Impact of different initialization methods on the quality of sea forecasts for the sicily channel, Journal of Operational Oceanography 9 (sup1) (2016) s119–s130. doi:10.1080/1755876X.2015.1114804.

7. Figures
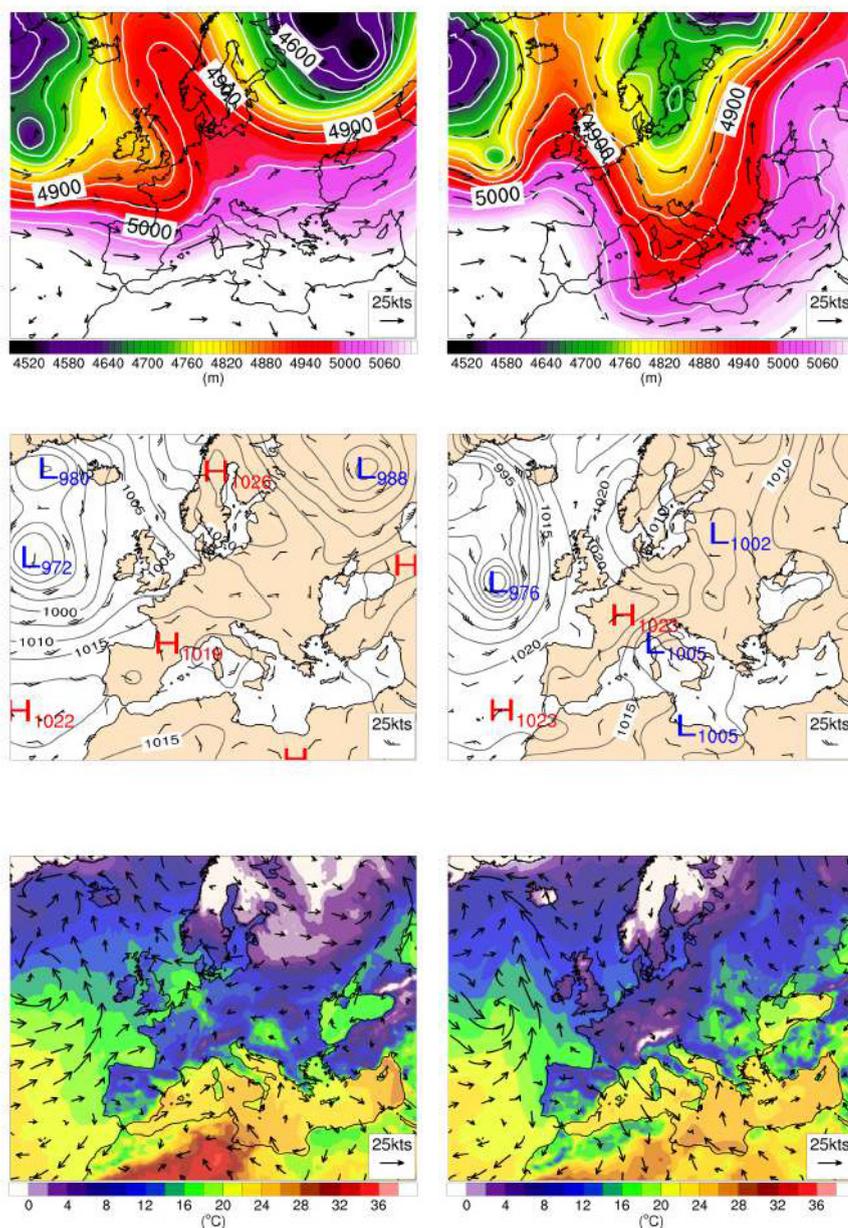
Figure 1: Synoptic situation at the begin and at the end of the 11 days period. Top, maps of geopotential heights at 500 Hpa for September 23 (left) and October 3, 2019. In the middle, the mean sea level pressure for the same dates. Bottom 2 m air temperature and 10 m averaged wind field.
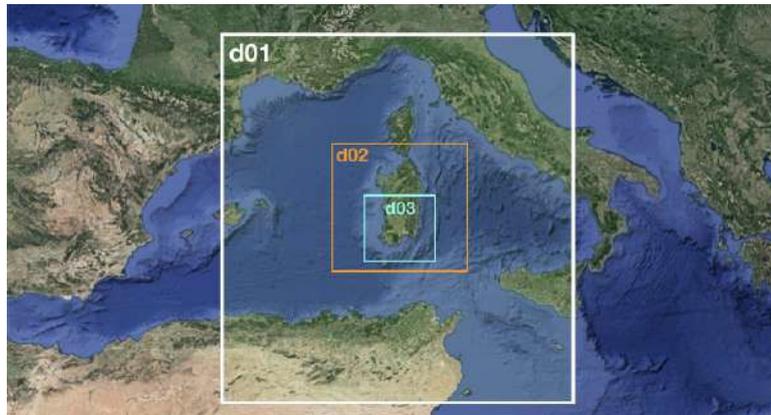
Figure 2: Model domains of MoSarT system.
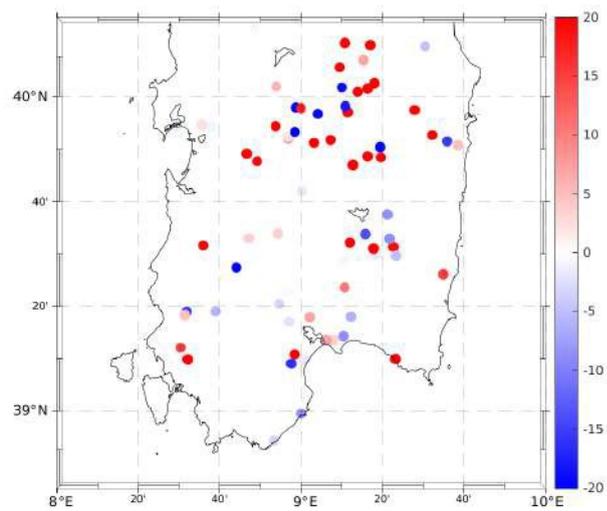
Figure 3: Differences of absolute quota biases for D3 domain between high and low resolution topography. Red means that the representation of stations is improved, blue means that is worse. Map units are meters.
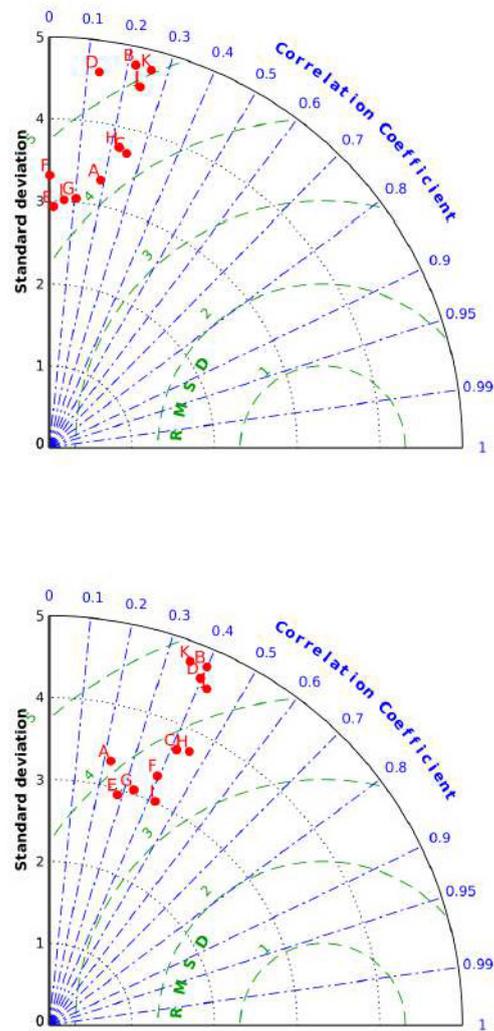
Figure 4: Taylor diagrams for wind intensities for D1 (top) and D3 (bottom) solutions. Labeled red dots are the 11 forecast days, A to K.
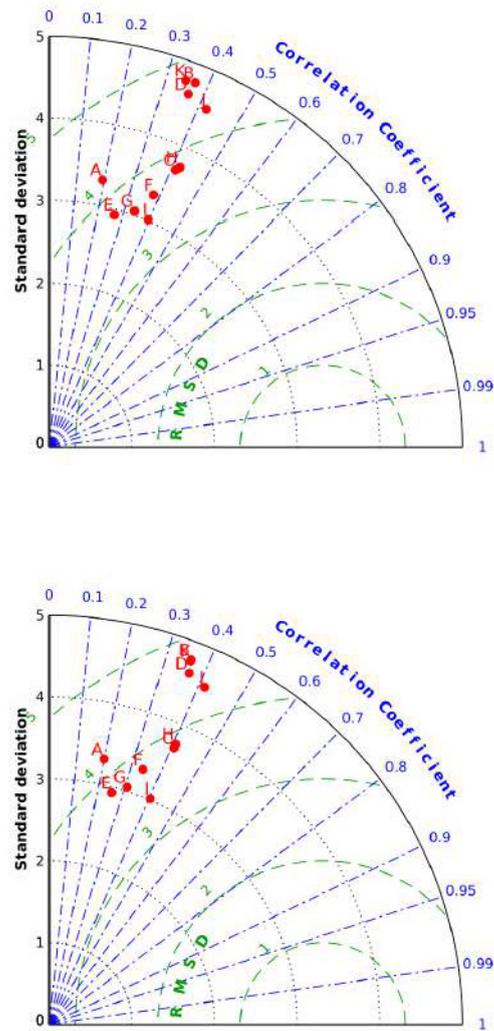
Figure 5: Taylor diagrams for wind intensities for D2nest (top) and D2stand (bottom) solu‐ tions. Labeled red dots are the 11 forecast days, A to K.
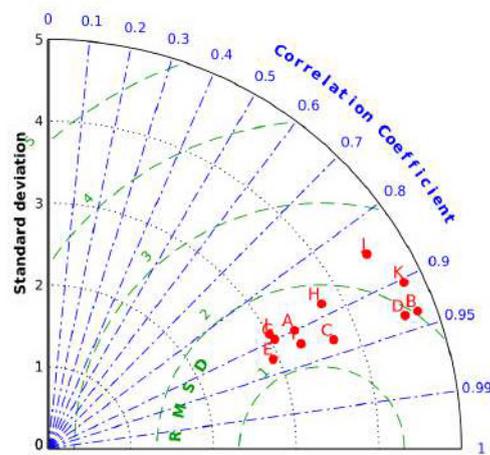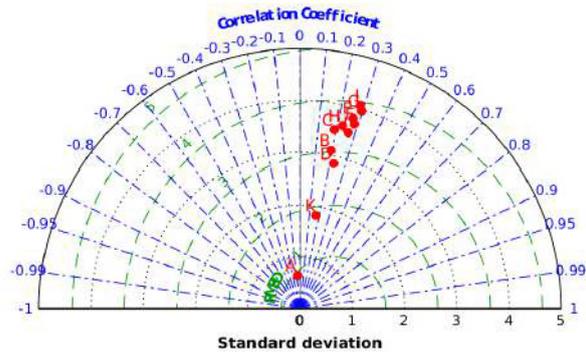
Figure 6: Taylor diagrams for 2 m air temperatures for D1 (top) and D3 (bottom) solutions. Labeled red dots are the 11 forecast days, A to K.
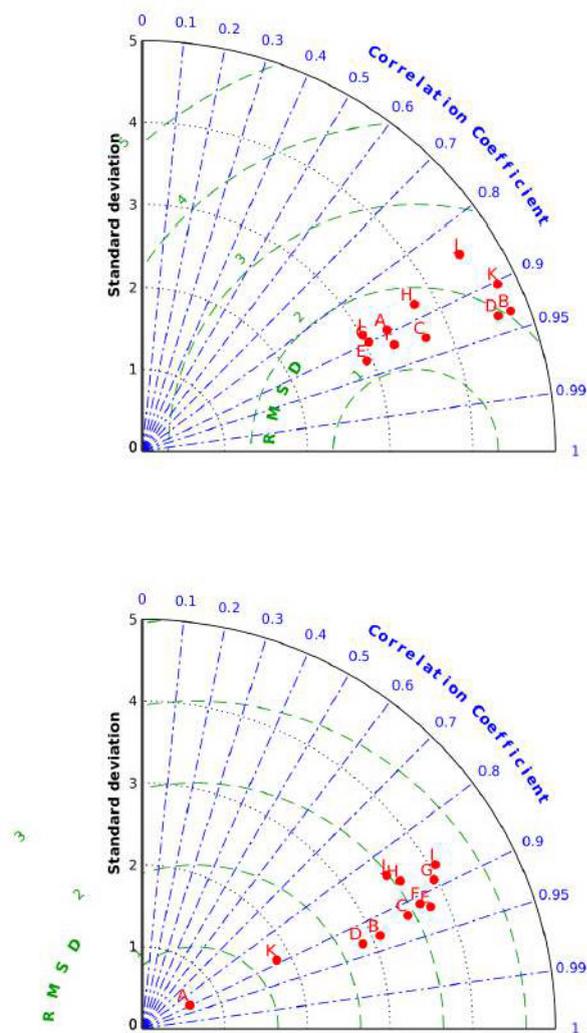
Figure 7: Taylor diagrams for $2m$ air temperatures for D2nest (top) and D2stand (bottom) experiments. Labeled red dots are the 11 forecast days, A to K.
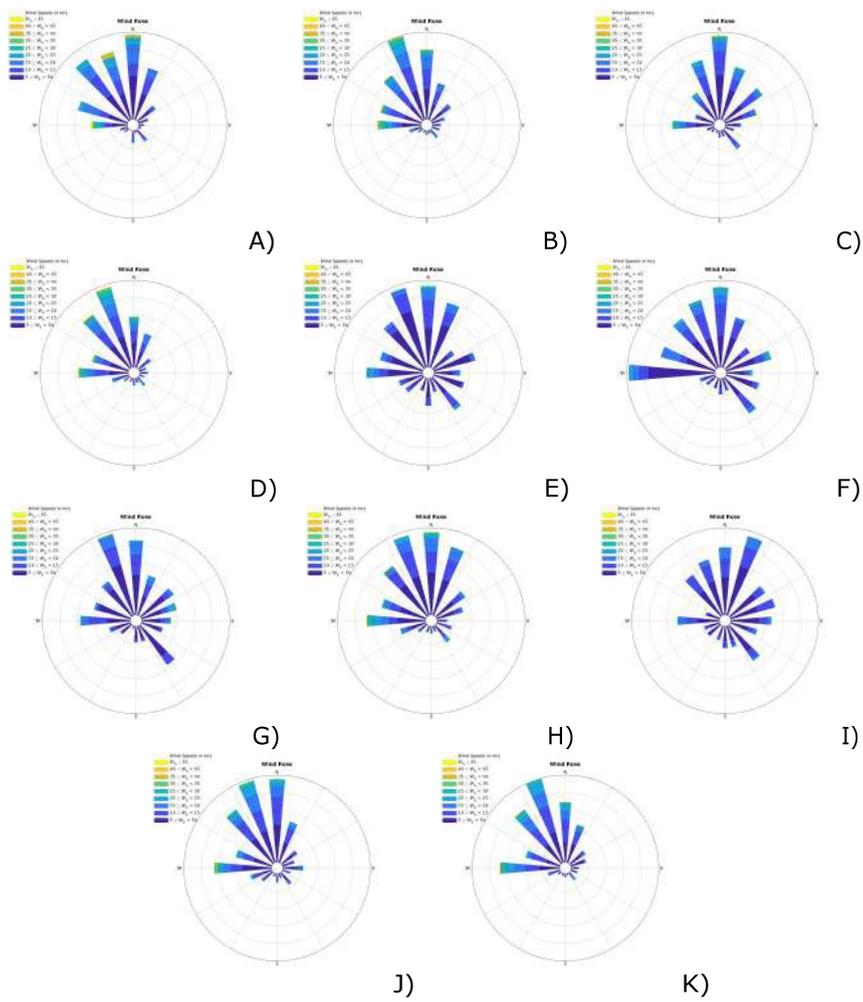
Figure 8: Wind directions for the 11 days of the experiments. Westerly (NW and SW) winds are largely prevalent over the entire period. A) to K) are the 11 forecast days.
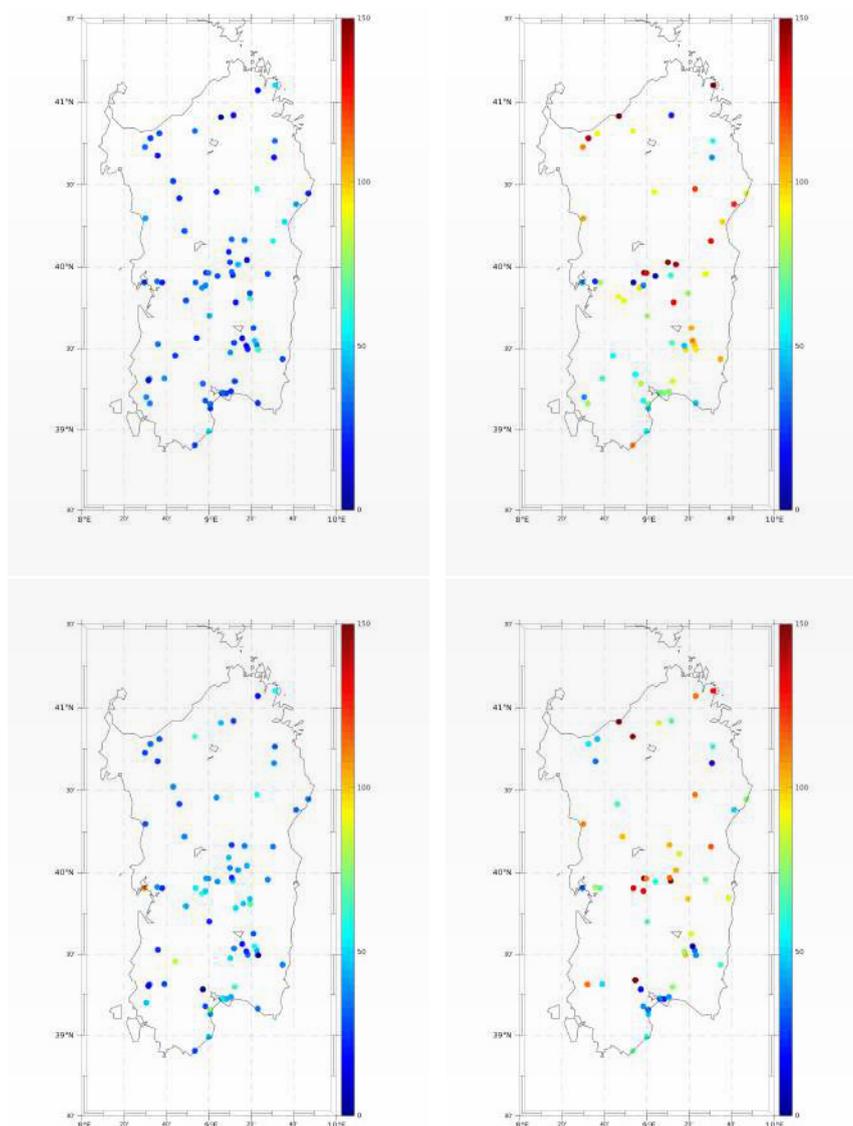
Figure 9: Maps of differences between observed and modeled $10m$ wind directions for the western sectors for the D2nest solution. Angles are in degrees. The four sectors are presented in geographical order, NW top left, NE top right, SE bottom right, SW bottom left.
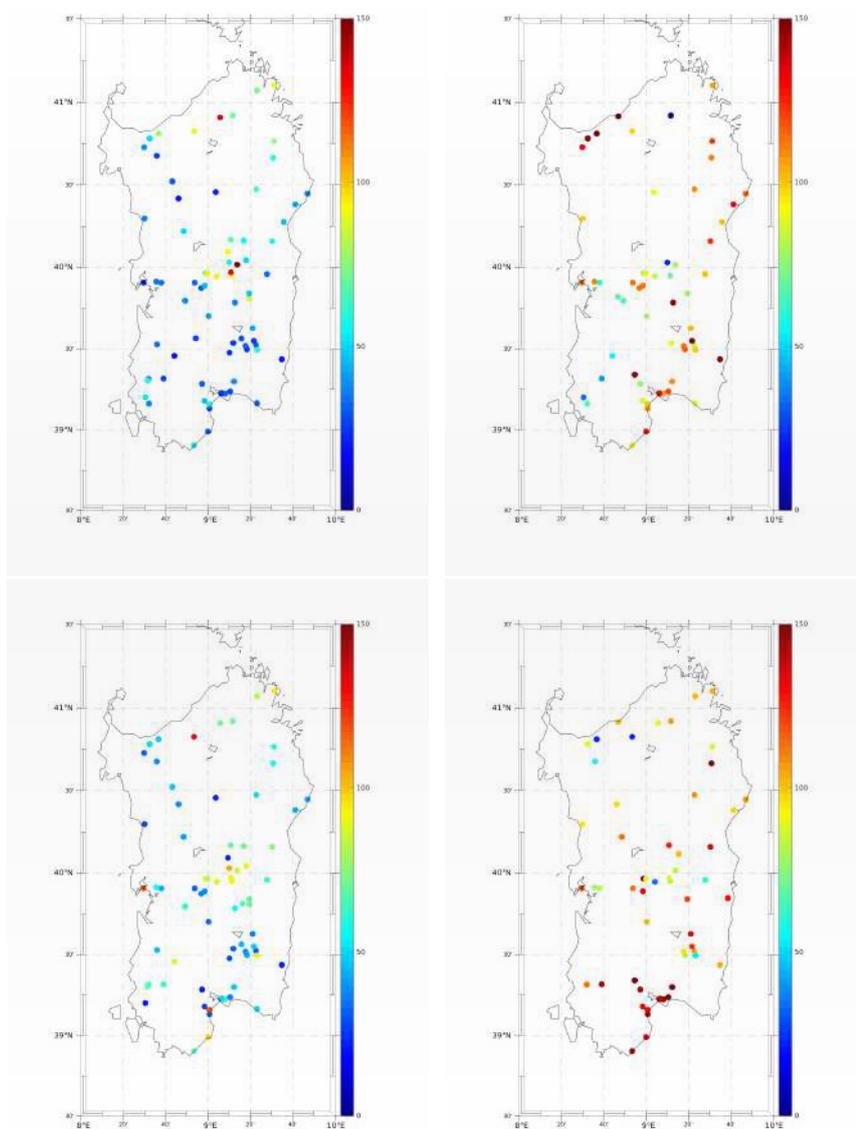
Figure 10: Maps of di↵erences between observed and modeled $10m$ wind directions for the western sectors for the D1 solution. Angles are in degrees. The four sectors are presented in

geographical order, NW top left, NE top right, SE bottom right, SW bottom left.

Effects of local and non-local PBL schemes on weather forecasts over a windy Mediterranean Island

Leopoldo Fazioli, Antonio Olita
ISAC-CNR

1. Introduction

Physics parameterizations are essentials to simulate the atmospheric dynamics, approximating the contribution of unresolved atmospheric processes for a given grid resolution in modeling applications. In this context, parameterizations are adopted to simulate a wide range of sub-grid processes as for instance the cumulus formation, the shortwave and longwave radiation, the microphysics of cloud formation and precipitation, land-atmosphere interface fluxes and the turbulence of Planetary Boundary Layers (PBL) (Stull, 1988, Stensrud, 2009).

In the short-range weather prediction, a key factor lies in parameterizing the turbulent motions into the PBL. Generated by thermal and mechanical processes of the atmosphere close to the surface, turbulent motions govern the mixing of heat, moisture and momentum influencing surface variables (i.e. temperature, relative humidity, winds), the vertical extent of atmospheric mixing and other processes such as the evolution of low clouds and rain. The parameterization of the turbulence into the PBL is based on the closing of the system of equations for a turbulent flow (Stull, 2012, Stensrud, 2009, Stull, 1988).   There are usually two kinds of approach to get the turbulence-closure problem: the 'local' and the 'non-local'.

In the local, the variables at a given point are affected by vertical layers symmetrically adjacent following the so-called K-theory. Dealing the turbulence similar to molecular diffusion, it is generally considered a small-eddy closure technique. Such schemes are usually of one-and-a-half order closure, by requiring one additional prognostic equation of the Turbulent Kinetic Energy (TKE) to determinate eddy diffusion coefficients and PBL height (Stull, 1988). PBL local closure schemes (e.g. Mellor & Yamada, 1974, 1982, Bougeault & Lacarrere, 1989, MYJ, MYNN2, BouLac) are often preferred in stable Stratified Boundary Layer(SBL) conditions (i.e. night-time) (Shin & Hong, 2011, Tyagi et al., 2018), using variables and parameters that are defined for each model level (e.g. local gradients). Despite the inability to directly represent transport between non-consecutive levels, local schemes attempt to resolve also the unstable Convective Boundary Layer (CBL) mixing by adding higher-order terms (Stull, 1991). This, however, may negatively affect the PBL height (PBLH) in CBL free convection conditions, producing too shallow PBLH and underestimating the interactions with upper atmosphere (as the entrainment of the free atmospheric air into the PBL) (Xie et al., 2012).

In the non-local approach, the parameterization is made by using known quantities at any of grid points, elsewhere in the vertical, while the diffusion coefficients depend on the PBL thickness. Hence, it assumes that larger-size eddies can transport fluid across finite distances before the smaller eddies come into play in mixing (Stull, 1988). Non-local closure schemes (e.g. Hong et al., 2006, Pleim, 2007, YSU, ACM2) are usually preferred for dominant CBL conditions (i.e. daytime), when surface heating and positive buoyancy fluxes generate thermal instabilities, turbulence and consequent convective motion. On the other hand, limits have been found in the production of an exceeding PBLH and the tendency to overestimate mixing in windy condition (Xie et al., 2012).

The present technical report aims at evaluating, across summer-winter period, the suitability of the non-local YSU diffusive PBL parameterization and of the local BouLac orographic-induced turbulence one for a WRF-ARW 1km local implementation, named MoSarT (Models of Sardinia Toolkit, currently operationally for forecasting). The focus is placed on verification of modeled surface air 2m-temperature and 10m wind speed and direction respect to measured data of 40 weather stations in terms of RMSE, BIAS and correlations indexes. An overview on the effects on predictability of precipitations is also made in probabilistic terms.

We aim to obtain an exhaustive statistic over a specific sub-region by verifying a limited number of variables over 6-months of simulation.

2. Study Area and Meteorological overview

Sardinia is the second largest island of the Mediterranean with an extension over the 24000 km2. The Island landscape is topographically heterogeneous, with a main elongated flat-land in the NW-SE direction, included in a basically rocky mountain terrain. Topography is complex, with deep and narrow canyons, valleys, some mountain higher than 1500 m and cliffs in many stretches of the coastline but especially along the eastern coast of the Island, where they can exceed 300 meters. Sardinia is characterized by a Mediterranean climate, with relatively mild winters and very hot and dry summers (Caloiero & Guagliardi, 2020, Beck et al., 2018). Throughout the year, the island is mainly exposed to westerly winds like the Libeccio (SW) and the prevailing Mistral (NW). Scirocco winds (SE) are also frequent. Our study area is limited (because of computational constraints) to the central and southern part of Sardinia island, crossed by the Campidano Plain (the above mentioned flatland). The Island is often subject to intense and extreme meteorological events, as the recent rainfall events that in 2021 interested some very local areas of the island (e.g. Prat et al., 2021, WRF-ARW model for short term rainfall forecasts of three severe storm cases in Italy). The island is also particularly exposed to high summer temperatures and heat waves (exceeding 40 degrees celsius). The period studied is of about 6 months, from August 2020 to January 2021. The observed hourly wind speeds

and directions are shown, month by month, by using circular diagrams in Fig.1. Monthly spatial averages were computed for temperature and wind speed. The number of significant rainy days (rain > 1mm/day for more than one station) and total accumulated precipitation were extracted for each month. As shown in tab.1, August was characterized by warmest 2m temperature

	Aug	**Sep**	**Oct**	**Nov**	**Dec**	**Jan**
aTemp	25.8	21.1	15.6	14.0	9.7	8.6
nRain	4	17	16	11	25	25
qRain	0.3	87.5	35.6	44.0	128.9	103.3
aSpeed	5.9	5.5	6.1	5.2	5.4	7.4
pDir	WNW	WNW	NW	NE	WNW	WNW

Table 1: Monthly averaged values of measured air temperature(aTemp) in C∘; number of rainy days in the month(nRain); based on nRain average of the accumulated in mm/month (qRain); monthly averaged wind speed(aSpeed) in m/s and the prevailing monthly wind direction(pDir). Values are computed on 40 pre-selected weather stations and refer to each month.

reaching up to 45C∘ moving towards the valleys of the inland, while September recorded rainfall for a total of 17 days. After October, with temperatures recording values exceeding the averaged values of the season and quantitative precipitations lower than in September month, in both November and December heavy rainfall were observed and recorded with few solution of continuity in the daily presence of some precipitation over the two months. In January, 2m air temperature decreased down to negative values on taller mountains, recording an averaged value of 8.6C∘. Westerly and North-Westerly winds are prevalent for every month took in consideration, while the dominants have been South- Easterly and North-Westerly respectively in November and January (Fig.1, panels D and F).

3. Methods and data

Model and experimental setup

MoSarT implementation used for this study is based on Advanced Weather Research and Forecasting model (WRF-ARW V4.2, released on April, 2020), a fully compressible, non-hydrostatic primitive equation limited-area model widely diffused in the atmospheric sciences community (Skamarock et al., 2019, 2008, 2005). In its present form, it consists of three two-way nested models with a Lambert conformal projection and regular grid sizes respectively of 9, 3 and 1 km, named d01, d02 and d03(Fig.2). Each nested domain is

entirely embedded in the lower resolution one. The domains are built by WRF pre-Processing System (WPS), using an higher resolution 3 sec topography(Fig.3). Such to- pography was then interpolated on the model grid resolution. This allowed a better representation of the weather stations and a lower representation error.

Unified Noah land-surface option is chosen to modeling land surface processes in numerical weather prediction (Tewari et al., 2004). Longwave and shortwave ra- diations are calculated using Rapid Radiative Transfer Model (RRTM) (Mlawer et al., 1997) and the Dudhia algorithm (Dudhia, 1989) respectively. Microphysic is the WRF Single-Moment 6-class scheme (Hong et al., 2004, WSM-6class), for all the three domains. The Kain-Fritsch scheme of cumulus is adopted only for the coarser domain (Kain, 2004), while the both inner domains itself solved explicity the cumuls cloud without any parameterization (Arakawa et al., 2011, Weisman et al., 1997). The PBL schemes used in the work are the first-order, non-local, YSU (Hong, 2010, Hong et al., 2006) and the 1.5-order, local closure scheme, BouLac (Bougeault & Lacarrere, 1989). The first uses a parabolic K-profile in an unstable mixed layer by adding an explicit term to manage the entrainment layer at the top of the PBL. The second employs a TKE prediction formulation to include the orography-induced turbulence into the parameterization. Initial and boundary conditions are obtained from hourly 0.25∘ NCEP (National Center for Environmental Prediction) Global Forecasting System (GFS) simulations (National Centers for Environmental Prediction, National Weather Service, NOAA, U.S. Department of Commerce, 2015). The MoSarT model is set up in forecast mode, performing, daily, 24 hrs starting at 00:00 UTC in slave-mode (e.g. Fazioli et al., 2016, impact of different initialization methods). We maintained the recommended 1 : 3 grid ratio while the number of vertical levels for each domain is 45. Validation concerned the d03 highest resolution domain.

Observations and Data processing

In order to evaluate model performances, we used a set of data derived by the observational network of the Sardegna Clima Onlus no-profit association. The association owns and/or indirectly maintain about 100 weather stations all over Sardinia. About 50 stations cover the d03 domain. Such stations were therefore used for the present paper. Data were processed to filter out outliers and bad values (e.g. temporary and/or accidental switch-off of the stations for more than 1-hour). The processing allowed to have an average of 40 stations per day available for the validation, never dropping below 34 stations per-day. During the 6-months of study period (from August 6th, 2020 to January 31st, 2021) only three days are missing due to insufficient data (i.e., October 13th, 2020; January 22nd and 23rd, 2021).

About rainfall validation, only 4-months (from September 1st, 2020 to December 31st, 2020) are considered, due to the lack of precipitation and to increase in inland snowfall in August and January,

respectively. The weather stations, of various type but ranging from semi-professional to professional in all cases, collected, at different time sampling ranging from few seconds to 5 minutes at most, temperature, wind speed and directions, relative humidity, atmospheric pressure and daily rain. For the present technical report we focus our attention to daily precipitation, to 10 m wind and 2 m temperature. In order to compare observations with model outputs, the observational values are linearly interpolated in time to the model output time vector. For winds, considering the problem of interpolating angles, we converted angular direction and magnitude of winds to U and V components, then we proceeded with the interpolation separately for U and V components; we re-converted obtained U and V data to module (magnitude) and angular direction. For what concern the co-location of stations with simulated values, we opted for the closest grid point to the actual position of the weather station, instead of averaging or interpolating values. In the next sub-section the metrics used for the evaluation are described.

Metrics

BIAS and RMSE, were separately computed in space and time between model outputs and observations. RMSE is the root mean square error between model and observation, while the BIAS is the Mean difference between the two. The latter represent the systematic error performed by the model in estimating a given physical quantity. Formulas are really not needed, as they are quite common metrics used in geophysics and can be retrieved everywhere. It is worthy to be noticed that the BIAS is positive (negative) for model overestimation (under-estimation). RMSE and BIAS have been computed for temperature, wind speed and wind directions. For latter, we verified models data through the method of absolute deviation of a circular variable by sampling the angles of $22.50°$. Positive and negative values represent a clockwise and anti-clockwise deviation in comparison with observations (Northern Hemisphere). Dispersion of the Error is given in terms of Standard Deviation(STD) by meaning low(high) errors like constant(random) closing to a correct(incorrect) solution also with high RMSE. In order to quantify the relative improvement of the RMSE in forecasts, another metric, namely the Relative Skill Score (Wilks, 2011) is employed. The relative skill score (RSS) is:

$$RSS = \frac{RMSE\_YSU - RMSE\_BouLac}{RMSE\_BouLac} 100$$

where $RMSE_{YSU}$ and $RMSE_{BouLac}$ mean to the error associated to YSU and BouLac PBL schemes, respectively. A positive (negative) RSS score implies that the BouLac technique improves (deteriorates) the

WRF forecasts with respect to the YSU one. By applying daily RSS to the temperature, wind speed and wind direction variables, we refer him as RSST, RSSW and RSSD respectively.

Categorical statistics

Real-time 24-h quantitative precipitation forecasts from two MoSarT operational setup are verified (McBride & Ebert, 2000) versus 40 rain gauges using the dichotomous approach and introducing the standard 2 x 2 contingency table of the events (Wilks, 2011). Multiple rain thresholds (i.e., 0.25, 1, 2, 5, 10, 20, 50 mm/day) separate "yes" and "no" events for both forecasts and observations. Validation results are evaluated for the 4 months: September,

October, November and December.

	OBSERVATIONS		
		YES	NO
FCST	YES	HITS	FALSE
	NO	MISS	REJECT

Table 2: Contingency table of events occurrences

In tab.2 the four entries are: correct forecasts of event occurring (HITS); event observed but not predicted (MISS); event predicted but not observed or false alarm (FALSE); correct forecasts of event not occurring (REJECT). The number of overall events of the contingent table is the sum of four entries (TOTAL). For reliable operation of a model, it would produce only HITS and REJECT, and no MISS or FALSE. Some commonly used statistics are adopted:

$$POD = \frac{1}{N}\sum_{i=1}^{N}\frac{HITS}{HITS + MISS}$$

$$FAR = \frac{1}{N}\sum_{i=1}^{N}\frac{MISS}{HITS + MISS}$$

$$SR = \frac{1}{N}\sum_{i=1}^{N}\frac{HITS}{HITS + FALSE}$$

$$FBI = \frac{1}{N}\sum_{i=1}^{N}\frac{HITS + REJECT}{HITS + MISS}$$

where N is the total number of rain gauges. Considering rainfall data based on 24-h accumulation(00:00-23:00UTC), the above indexes represent the N-averaged Probability Of Detection, False Alarm Rate, Success Ratio and Frequency Bias Index respectively (POD, FAR, SR, FBI). The first three indexes assess the probability (%) that a given event will occur event; the last one ranges from 0 to infinite and provides information of overestimation or underestimation with FBI>1, FBI<1 respectively. For FBI=1 we have a "perfect" score, i.e. forecast and observations provide identical values.

4. Results

We remind here that the aim of the paper is to investigate the differences in forecasting surface wind, temperature and daily rainfall given by the alternative use of BouLac and YSU parameterization schemes of PBL. So, the purpose is to identify which one is more suitable for our Area of Interest. Our primary attention focused on the trend of the errors and skill scores during the period through the analysis of time series. This allowed to detect the days with largest differences, on which we focused (test cases) to understand such differences more in depth. Such cases were analyzed to investigate the spatial distribution of the error over the area, including wind directions that, at first, were not took into account. The following Tab.3 summaries the monthly RMSE of both experiments for temperature, wind speed and precipitation. About the latter parameter, a shorter period was considered, as explained in the Section 3.2.

RMSE	Aug	Sep	Oct	Nov	Dec	Jan
TEM-L	2.340	1.600	1.379	1.330	1.290	1.200
TEM-N	2.360	1.620	1.440	1.390	1.350	1.320
WSP-L	3.530	3.190	3.450	2.860	3.180	4.040
WSP-N	3.500	3.180	3.450	2.870	3.140	4.060
RAIN-L	-	8.104	2.359	7.393	6.787	-
RAIN-N	-	8.100	2.239	6.431	6.572	-

Table 3: Monthly RMSE of temperature(C∘), wind speed(m/s) and accumulated daily precipitation (mm) using local(-L) and non-local(-N) PBL scheme.

In order to improve the model capability to better resolve the complex topography, a relevant improvement in the model setup was to provide a more detailed description of the terrain for d02 and d03 domains by introducing a higher resolution topography (3 sec).

Temperature and wind skill assessment

Monthly temperature and wind speed RMSE are shown in Tab.3. The RMSE differences between the two are in the order of about $10−1$ for the temperature and $10−2$ for the wind speed. The temperature RMSE showed a decrease August to January, ranging the RMSE from about 2.4 C◦ in August to 1.2 C◦ in December and January, accordingly with a lower diurnal variation. That of wind ranged from about 2.8 to 4 m/s, mainly depending by frequency and intensity of windy events. Daily RSS, as above described, is shown in Fig.5. RSST and RSSW refer to the temperature and wind speed respectively. On 176 total available days, 111 were on which RSST was positive, 52 on which it was negative and the 9 remaining were about zero. Instead, RSSW were positive, negative and neutral in 50, 111 and 15 days respectively. The absolute value of both relative skill scores appears to increase at windy conditions, especially with regard to RSST. In Fig.6, a summary graph relates observed daily spatial averaged 10 m wind speed and RSST. Such index fluctuates between positive and negative values for wind speeds lower than 5 m/s, with maximum density (red filled circles) around a value of 5%. For observed wind speed values greater than 7 m/s, the RSST grows linearly with those of wind speed, reaching values up to 30%. The positive linear regression is shown by a red line.

Test case

During the entire 6-month period we found daily maximum and minimum of RSST and RSSW in corresponding of windy events. January 9th and 14th, 2021, are chosen as significant relevant days based on the lowest and highest values of RSST observed in Fig.5. January 14th, was characterized by dominant northern and western winds through- out the 24 hours flowing up to 30 m/s(Fig.6, panel A). During January 9, the southern and eastern hourly winds blew lower and were characterized by a large variability in the directions (Fig.7, panel B). Modeled hourly time series for January 14th(Fig.7, C and E) and January 9th(Fig.7, D and F) are shown for local and non-local schemes. The daily maps in Fig.8 show the spatial distribution of RSST, RSSW and RSSD at the active stations. In January 14, we found a clear prevalence of positive RSST (Fig.8, A), reaching a maximum of 70% and a spatial average of about 27%. The locally RSSD reached a value of 90%. In terms of spatial average we obtained the RSSD close to 10%(Fig.8, panel E) and the RSSW weakly positive of about 3%(Fig.8, panel C). In January 9, RSST were overall negatives with an average of -31% and a minimum of about -100% (Fig.8, B). RSSW and RSSD were almost exclusively negatives, especially the former. Averaged values for both RSSW and RSSD are about -7% (Fig.8, D and F).

Rainfall verification

Monthly RMSE of precipitations in mm are shown in tab3. During September, the RMSE was of about 8.1 mm using both schemes. In October, RMSE shows lower values compared to the other months for both the schemes, probably because of the lack of heavy rainy events. Largest RMSE difference of about 0.9 was in November. More in general, the best performances for precipitations in terms of RMSE is reached with the non-local scheme. In Fig.9 the scatter plot of the entire period for precipitations shows a summary of the differences between observed and modeled rainfall. Despite a then non-local scheme shows a lower RMSE (6.23 mm) in respect to the local one (6.57 mm), the fit of the red-line in top panel of Fig.9 suggest a better linear correlation for the second. In facts, the r2 is 0.704 and 0.692 respectively by for local and non-local scheme. To further quantify the model's performance in rainfall forecasting, the probability of events occurrences using predefined thresholds is shown in Fig.10. An evaluation of the probability indices is provided for each month. Worst performances of the model are shown in September for both setups. POD by using local scheme is higher than the non-local one, especially for thresholds from 0.25 to 5 mm (panel A). In October, characterized by a lack of heavy rainfall, the FAR exceeded 50% for both methods; POD of non-local experiment was larger for the thresholds 1 and 2 mm (panel B). In November, POD and SR increased (panels C), especially in local scheme, by reaching both indexes up to 70% for thresholds from 1 to 10 mm. Corresponding on 1, 2 and 20 mm thresholds, local experiment produces better scores, well summarized by higher SR. In December, rainiest month among those analyzed, we obtained overall appreciable scores: POD keep to stay higher than 50% using local scheme, while decreased on threshold 10 and 20 using non-local one; FAR was lower than the other months and increased going toward higher thresholds for both runs; SR decreasing with the increase of threshold values, despite a 100% of False Alarm concerning a single event over 50 mm/day (panel D). About FBI, the non-local method over-forecasts (more than the local one) the two higher thresholds in September and for the 2mm threshold in October. Non-local values further improve in October, approaching the value of 1 November. In December, we observe comparable FBI provided by using both PBL schemes, getting closer to observations, excepts for the very large value reached for the threshold of 20 mm.

In the following table 4, a 6-months synthesis of probabilistic indexes based on rain thresholds.

	POD	FAR	SR	FBI
Thershold	Loc-Non	Loc-Non	Loc-Non	Loc-Non
0.25	47-44	45-44	55-56	0.98-0.85
1	55-56	44-43	56-57	0.95-0.86
2	54-50	39-45	61-55	1.00-1.07
5	50-49	44-44	56-56	1.06-0.91
10	42-39	54-52	46-48	0.97-0.90
20	46-32	65-64	35-36	1.70-1.74
50	48-48	92-88	8-12	1.87-1.82

Table 4: Probabilistic indexes of POD, FAR and SR (%) of model performance in forecasting rainfall using local and non-local schemes. FBI>1, FBI<1 or FBI=1 refer to over forecasting, under forecasting or on desirable perfect score respectively. Averaged values refer to the entire period (from September to December, 2020).

5. Summary and Conclusions

In this work, a 2-way WRF multiple domain model, named MoSarT, for weather forecasting over the Sardinia region (Western Mediterranean), was setup and run in forecast mode at 9, 3 and 1 km of spatial resolution (d1, d2 and d3 respectively). Two different setup for what concerns the PBL were run, in order to identify the condition on which the two, a local and a non-local scheme, were better performing over the region. The d2 and d3 topography were improved through the use of the SRTM high resolution data-set. The finest application, which covers southernmost 3/4 of the Island, was verifiedover a period of 6-months(August-January) against reference surface air temperature and wind speed provided by the network of weather stations owned by Sardegna Clima Onlus. The daily precipitation was analyzed during a shorter period of 4-months (September-December). As above mentioned, MoSarT was run twice using a local and a non-local parameterization scheme of the PBL, more specifically the BouLac (Bougeault & Lacarrere, 1989) and YSU (Hong, 2010) respectively. Modeled daily results were evaluated mainly through basic statistics of the errors (RMSE) on 10 m wind speed, 2 m air temperature and rainfall. Since each season in Western Mediterranean Sea is usually affected by different type and entity of rainfall (Insua-Costa et al., 2021), total daily precipitations were also validated, month by month, through the verification of the events occurrence in probabilistic terms. Daily Relative Skill Scores of temperature (RSST), wind speed (RSSW) and direction (RSSD), were adopted to quantify the relative improvement (in

%) of one PBL implementation in respect to the other. Positive (negative) values indicate higher (lower) relative performances of the local PBL in respect to the non-local one. The daily time series shows positive RSST in 65% and negative RSSW in 63% of the days (over a total of 176 days). It means that the a) local and b) non-local schemes better performed in forecasting a) temperature and b) wind speed, respectively. An even more significant consideration can be done by defining wind speed thresholds, as summarized in the following Tab.5. Under weak winds regime, most of the low wind speed error are associated to the non-local scheme. On the other side, by increasing the wind speed threshold, we observe an increase of low-error days by using the local scheme, for both temperature and wind speed. When the daily averaged wind is larger than 11 m/s, the local scheme provided the best model performances in the 100% of cases for both variables. This is an extremely relevant information considering that Sardinia is largely characterized by windy weather, as mentioned in the Introduction.

Wsp	n-days	n-temp		n-wind	
		Loc	Non	Loc	Non
<5	81	43	31	9	64
>5	86	62	17	39	40
>7	36	32	4	26	9
>9	17	17	0	16	1
>11	7	7	0	7	0

Table 5: Number of days with best skill score of temperature(n-temp) and wind speed(n-wind) obtained by using Local(Loc) and Non-local(Non) PBL scheme; daily average thresholds of measured wind speed(Wsp) are fixed and total number of days(n-days) in each included is given.

The spatial distribution of RSST, RSSW and RSSD in two significant test-cases, selected in virtue of the largest RMSE error recorded for such days, showed mainly negatives values (i.e. better performances for YSU scheme) during pre- vailing eastern and south-easterly winds and mainly positives during dominant north-westerly winds (i.e. better performances of Boulac). About RMSE of daily accumulated precipitation, we found an overall lower value by using the non-local scheme. On the other side, the local scheme shows a stronger correlation. i.e. a better linear fitting in respect to the non-local scheme. In terms of monthly

probabilistic indexes, it is evident that both runs poorly performed in September, with SR and POD under 50% for each thresh- old. SR and POD improved in October, still characterized by weak precipi- tations in terms of heavy events. Best performances found in November and December, SR and POD reaching 75%. FBI wavers across the runs, months and thresholds. Non-local FBI was disadvantageous in September and October, with a prevalent over-forecasting. It however is more performing by remaining closer to the perfect score (1) than the one computed by local scheme in November, when heavy precipitations substantially increased. In December, the rainiest month, was characterized by FBI close to 1 for both. The generally bad performances of the model in detecting rain in September-October, is probably due to the spatio-temporal scales of the heavy rain and of the rain in general. Heavy precipitation events are often characterized by short-time scales(1-2h) and very localized in space (few km2), which make the rain gauges spatial distribution insufficient to match the events and correctly collect data. In windy days, the temperature and wind speed were predicted better using local PBL scheme (lower RMSE). This can be explained thanks to the BouLac scheme peculiarity. The Bougeault–Lacarrere formulation of the TKE was written to include the additive effect of the orography-induced turbulence in the parameterization. It was found that in that way such parameterization better represent the PBL in regimes of high static stability in respect to non-local schemes like the YSU, which instead could produce too deep PBLH by overestimating the mixing in windy conditions (Xie et al., 2012, Shin & Hong, 2011). On the basis of our results, well synthesized in table 5, and considering that Sardinia is largely characterized by westerly windy weather conditions throughout the year (Montaldo & Sarigu, 2017), we may conclude that for our area of interest the PBL local (BouLac) scheme allows a better representation of near-surface temperature and winds in the MoSarT implementation. Despite a general better non-local (YSU) behavior in rain prediction (RMSE), the local scheme seems to ensure even higher performances in forecasting short but intense periods of rain in probabilistic terms, e.g. during the summer-autumn transition period (Mill′ an et al., 1995). As a future development of the present work, we will evaluate the possibility to include an ocean/wave model into the MoSarT forecasting system (Warner et al., 2010). Through the exchange of heat flows, the ocean forecast will dynamically compute by providing a feedback to the atmosphere model. This upgrade, although computationally expensive, could significantly improve our system, specially in forecasting extreme events most depended by the sea.

6. References

- Arakawa, A., Jung, J.-H., & Wu, C.-M. (2011). Toward unification of the multiscale modeling of the atmosphere. Atmospheric Chemistry & Physics Discussions, 11.

- Avolio, E., Stefano, F., Miglietta, M., Lo Feudo, T., Calidonna, C., & Sempre-viva, A. M. (2017). Sensitivity analysis of wrf model pbl schemes in simulating boundary-layer variables in southern italy: An experimental campaign. Atmospheric Research, 192, 58–71. doi:10.1016/j.atmosres.2017.04.003. Banks, R. F., & Baldasano, J. M. (2016). Impact of wrf model pbl schemes on air quality simulations over catalonia, spain. Science of the total environment, 572, 98–113.

- Beck, H. E., Zimmermann, N. E., McVicar, T. R., Vergopolan, N., Berg, A., & Wood, E. F. (2018). Present and future ǩoppen-geiger climate classification maps at 1-km resolution. Scientific data, 5 , 1–12.

- Borge, R., Alexandrov, V., Del Vas, J. J., Lumbreras, J., & Rodrˊıguez, E. (2008). A comprehensive sensitivity analysis of the wrf model for air quality applications over the iberian peninsula. Atmospheric Environment, 42, 8560–8574.

- Bougeault, P., & Lacarrere, P. (1989). Parameterization of orography-induced turbulence in a mesobeta–scale model. Monthly weather review, 117, 1872–1890.

- Caloiero, T., & Guagliardi, I. (2020). Temporal variability of temperature extremes in the sardinia region (italy). Hydrology, 7, 55.

- Carvalho, D., Rocha, A., Gomez-Gesteira, M., & Santos, C. S. (2014). Stull2012introduction sensitivity of the wrf model wind simulation and wind energy production estimates to planetary boundary layer parameterizations for onshore and offshore areas in the Iberian peninsula. Applied Energy, 135, 234–246.

- Chan, K. M., & Wood, R. (2013). The seasonal cycle of planetary boundary layer depth determined using cosmic radio occultation data. Journal of Geophysical Research: Atmospheres, 118, 12–422.

- Cheng, F.-Y., Chin, S.-C., & Liu, T.-H. (2012). The role of boundary layer schemes in meteorological and air quality simulations of the taiwan area. Atmospheric environment, 54, 714–727.

- Dudhia, J. (1989). Numerical study of convection observed during the winter monsoon experiment using a mesoscale two-dimensional model. Journal of the atmospheric sciences, 46 , 3077–3107.

- Fazioli, L., Olita, A., Cucco, A., Tedesco, C., Ribotti, A., & Sorgente, R. (2016). Impact of different initialisation methods on the quality of sea forecasts for the sicily channel. Journal of Operational Oceanography, 9 , s119–s130. doi:10. 1080/1755876X.2015.1114804.

- Furberg, M., Steyn, D., & Baldi, M. (2002). The climatology of sea breezes on sardinia. International Journal of Climatology: A Journal of the Royal Meteorological Society, 22, 917–932.

  Garcıa-Dıez, M., Fernˊandez, J., Fita, L., & Yag̈ue, C. (2013). Seasonal dependence of wrf model biases and sensitivity to pbl schemes over Europe. Quarterly Journal of the Royal Meteorological Society, 139, 501–514.

- Hong, S.-Y. (2010). A new stable boundary-layer mixing scheme and its impact on the simulated east asian summer monsoon. Quarterly Journal of the Royal Meteorological Society, 136 , 1481–1496.

- Hong, S.-Y., Dudhia, J., & Chen, S.-H. (2004). A revised approach to ice micro- physical processes for the bulk parameterization of clouds and precipitation. Monthly weather review , 132 , 103–120.

- Hong, S.-Y., Noh, Y., & Dudhia, J. (2006). A new vertical diffusion package with an explicit treatment of entrainment processes. Monthly weather review, 134, 2318–2341.

- Insua-Costa, D., Lemus-Ćanovas, M., Miguez-Macho, G., & Llasat, M. C. (2021). Climatology and ranking of hazardous precipitation events in the western mediterranean area. Atmospheric Research, 255, 105521.

- Kain, J. S. (2004). The kain–fritsch convective parameterization: an update. Journal of applied meteorology, 43 , 170–181.

- Lavagnini, A., Sempreviva, A. M., Transerici, C., Accadia, C., Casaioli, M., Mariani, S., & Speranza, A. (2006). Offshore wind climatology over the Mediterranean basin. Wind Energy: An International Journal for Progress and Applications in Wind Power Conversion Technology, 9, 251–266.

- McBride, J. L., & Ebert, E. E. (2000). Verification of quantitative precipitation forecasts from operational numerical weather prediction models over Australia. Weather and Forecasting, 15, 103–121.

- Mellor, G. L., & Yamada, T. (1974). A hierarchy of turbulence closure models for planetary boundary layers. Journal of Atmospheric Sciences, 31, 1791–1806.

- Mellor, G. L., & Yamada, T. (1982). Development of a turbulence closure model for geophysical fluid problems. Reviews of Geophysics, 20, 851–875.

- Millan, M., Estrela, M. J., & Caselles, V. (1995). Torrential precipitations on the spanish east coast: the role of the mediterranean sea surface temperature. Atmospheric Research, 36 , 1–16.

- Mlawer, E. J., Taubman, S. J., Brown, P. D., Iacono, M. J., & Clough, S. A. (1997). Radiative transfer for inhomogeneous atmospheres: Rrtm, a validated correlated-k model for the longwave (paper 97jd00237). JOURNAL OF GEOPHYSICAL RESEARCH-ALL SERIES-, 102, 16–663.

- Montaldo, N., & Sarigu, A. (2017). Potential links between the north atlantic oscillation and decreasing precipitation and runoff on a Mediterranean area. Journal of Hydrology, 553, 419–437.

- National Centers for Environmental Prediction, National Weather Service, NOAA, U.S. Department of Commerce (2015). Ncep gfs 0.25 degree global forecast grids historical archive. URL: https://doi.org/10.5065/D65D8PWK.

- Nezhad, M. M., Heydari, A., Groppi, D., Cumo, F., & Garcia, D. A. (2020). Wind source potential assessment using sentinel 1 satellite and a new forecasting model based on machine learning: A case study sardinia islands. Renewable Energy, 155, 212–224.

- Olita, A., Ribotti, A., Fazioli, L., Perilli, A., & Sorgente, R. (2013). Surface circulation and upwelling in the sardinia sea: A numerical study. Continental Shelf Research, 71 , 95–108.

- Pleim, J. E. (2007). A combined local and nonlocal closure model for the atmospheric boundary layer. part i: Model description and testing. Journal of Applied Meteorology and Climatology, 46 , 1383–1395.

- Prat, A. C., Federico, S., Torcasio, R. C., Fierro, A. O., & Dietrich, S. (2021). Lightning data assimilation in the wrf-arw model for short-term rainfall forecasts of three severe storm cases in italy. Atmospheric Research, 247 , 105246.

- Shin, H. H., & Hong, S.-Y. (2011). Intercomparison of planetary boundary-layer parametrizations in the wrf model for a single day from cases-99. Boundary-Layer Meteorology, 139 , 261–281.

- Skamarock, W., Klemp, J., Dudhia, J., Gill, D., Barker, D., Wang, W., & Powers, J. (2005). A Description of the Advanced Research WRF Version 2. Technical Report. doi:10.5065/D68S4MVH.

- Skamarock, W. C., Klemp, J. B., Dudhia, J., Gill, D. O., Barker, D. M., Wang, W., & Powers, J. G. (2008). A description of the advanced research wrf version 3. ncar technical note-475+ str, .

- Skamarock, W. C., Klemp, J. B., Dudhia, J., Gill, D. O., Liu, Z., Berner, J., Wang, W., Powers, J. G., Duda, M. G., Barker, D. M. et al. (2019). A description of the advanced research wrf model version 4. National Center for Atmospheric Research: Boulder, CO, USA, (p. 145).

- Stensrud, D. J. (2009). Parameterization schemes: keys to understanding numerical weather prediction models. Cambridge University Press.

- Stull, R. B. (1988). An introduction to boundary layer meteorology volume 13. Springer Science & Business Media.

- Stull, R. B. (1991). Static stability—an update. Bulletin of the American Meteorological Society, 72 , 1521–1530.

- Stull, R. B. (1993). Review of non-local mixing in turbulent atmospheres: Transilient turbulence theory. Boundary-Layer Meteorology, 62 , 21–96.

- Stull, R. B. (2012). An introduction to boundary layer meteorology volume 13. Springer Science & Business Media.

- Tewari, M., Chen, F., Wang, W., Dudhia, J., LeMone, M., Mitchell, K., Ek, M., Gayno, G., Wegiel, J., & Cuenca, R. (2004). Implementation and verification of the unified noah land surface model in the wrf model. In 20th conference on weather analysis and forecasting/16th

conference on numerical weather prediction (pp. 2165–2170). American Meteorological Society Seattle, WA volume 1115.

- Tyagi, B., Magliulo, V., Finardi, S., Gasbarra, D., Carlucci, P., Toscano, P., Zaldei, A., Riccio, A., Calori, G., D'Allura, A. et al. (2018). Performance analysis of planetary boundary layer parameterization schemes in wrf modeling set up over southern italy. Atmosphere, 9 , 272.

- Warner, J. C., Armstrong, B., He, R., & Zambon, J. B. (2010). Development of a coupled ocean–atmosphere–wave–sediment transport (coawst) modeling system. Ocean modelling, 35 , 230–244.

- Weisman, M. L., Skamarock, W. C., & Klemp, J. B. (1997). The resolution dependence of explicitly modeled convective systems. Monthly Weather Review, 125, 527–548.

- Wilks, D. S. (2011). Statistical methods in the atmospheric sciences volume 100. Academic press. Xie, B., Fung, J. C., Chan, A., & Lau, A. (2012). Evaluation of nonlocal and local planetary boundary layer schemes in the wrf model. Journal of Geophysical Research: Atmospheres, 117.

7. Figures
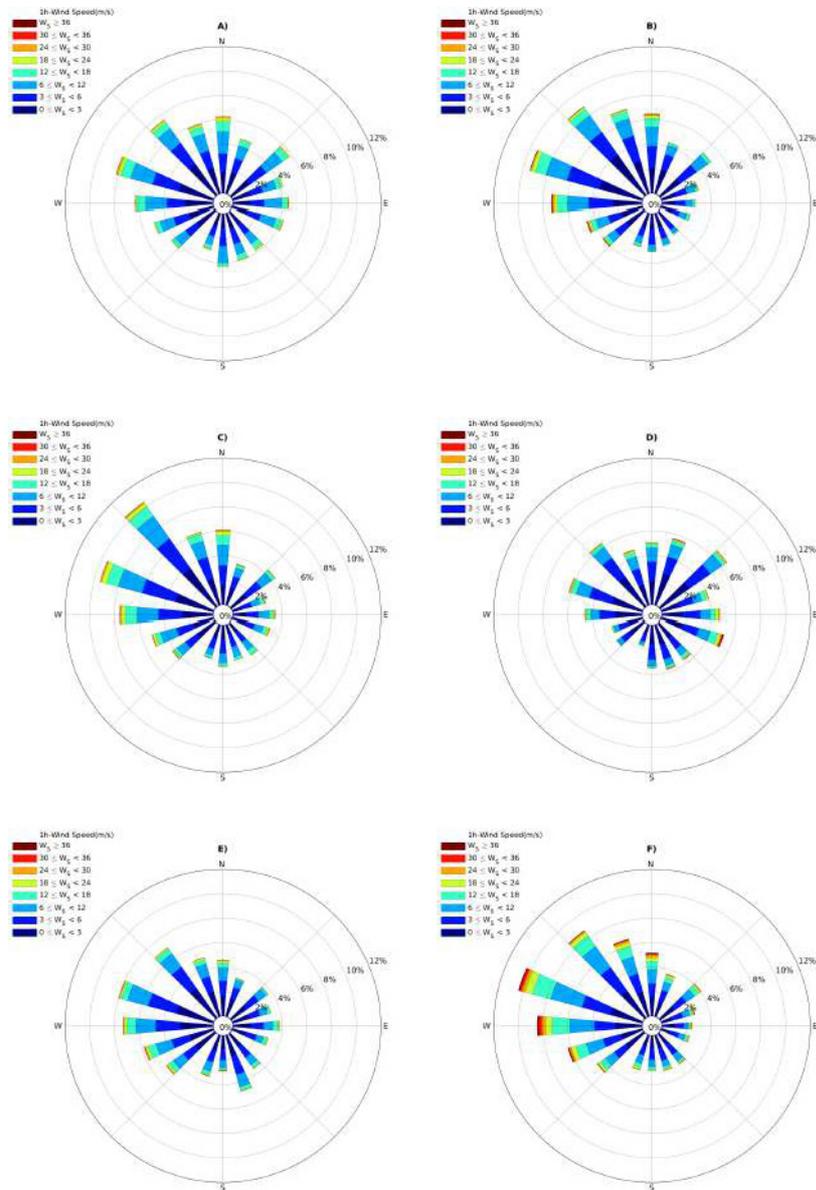
Figure 1: Hourly wind speedm/s and directions observed from the entire network of stations. Panels from A) to F) are rose diagrams, grouped by month from respectively August to January.
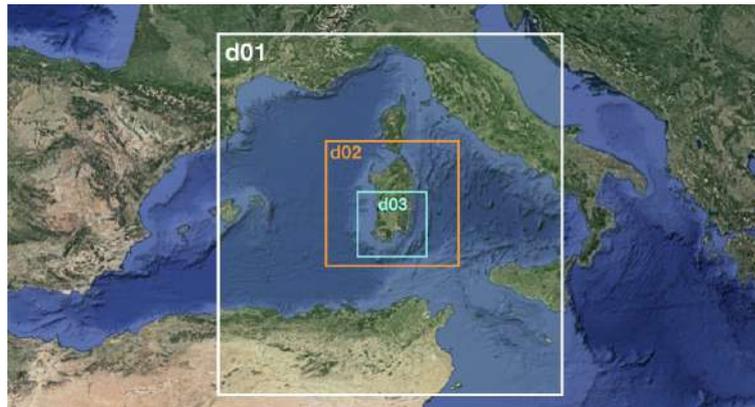
Figure 2: Model domains of MoSarT system.
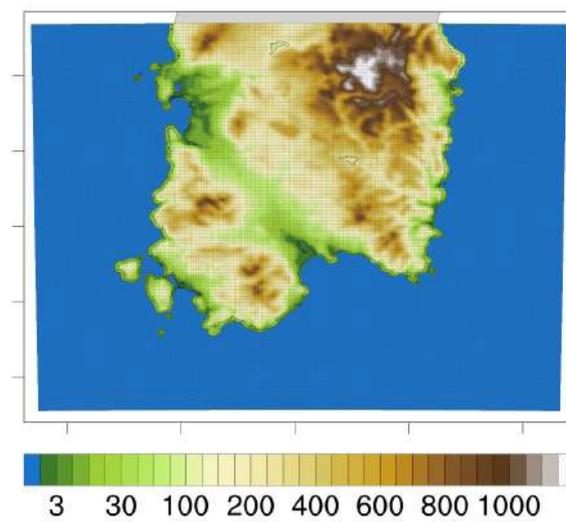
Figure 3: High resolution upgraded topography of MoSarT 1km domain.
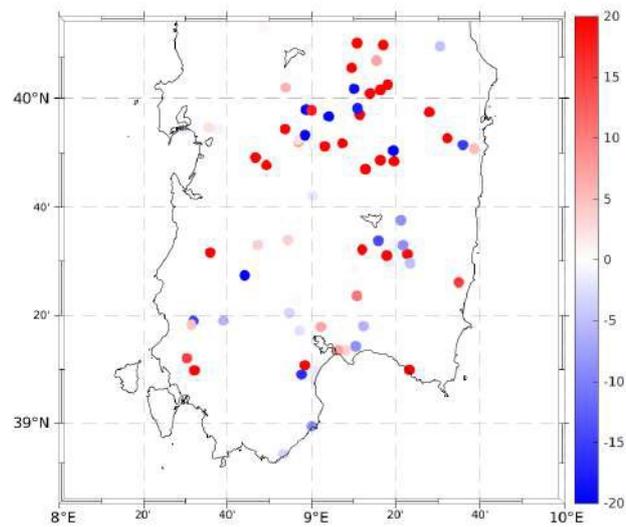
Figure 4: Differences of absolute quota biases for d03 domain between high and low resolution topography. Red means that the representation of stations is improved, blue means that is worse. Map units are meters.
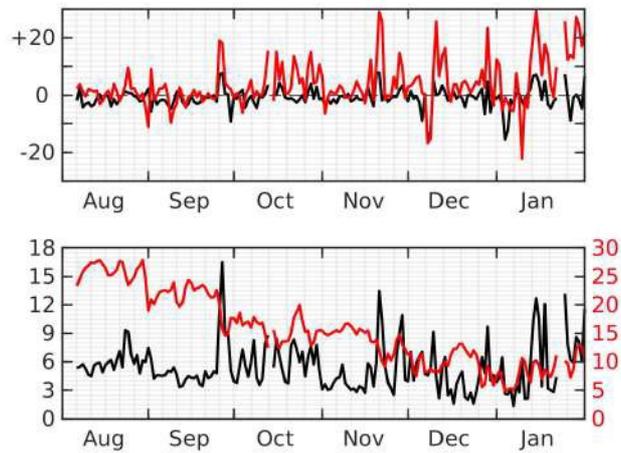
Figure 5: In top panel, the time-series of RSSW(black line) and RSST(red line) in %; positive(negative) values mean higher performances for BouLac(YSU) scheme. In bottom panel, the time-series of measured spatial averaged daily wind speed(black line) in m/s and measured spatial averaged daily air temperature(red line) in C^o
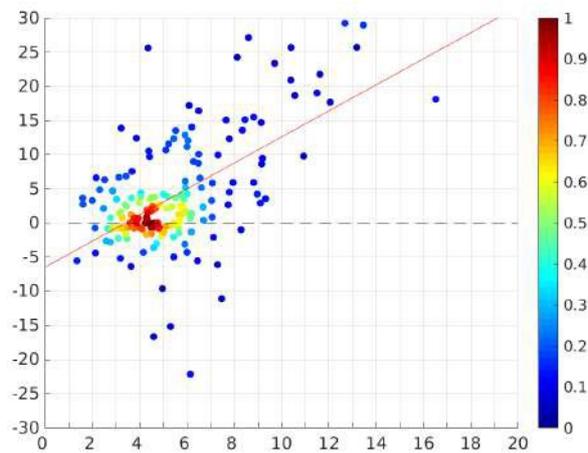
Figure 6: Linear regression between observed $10m$ averaged wind speed(abscissa) and RSST(ordinate). Colors of filled circles indicate the density of daily RSST; red means maximum, blue the minimum.
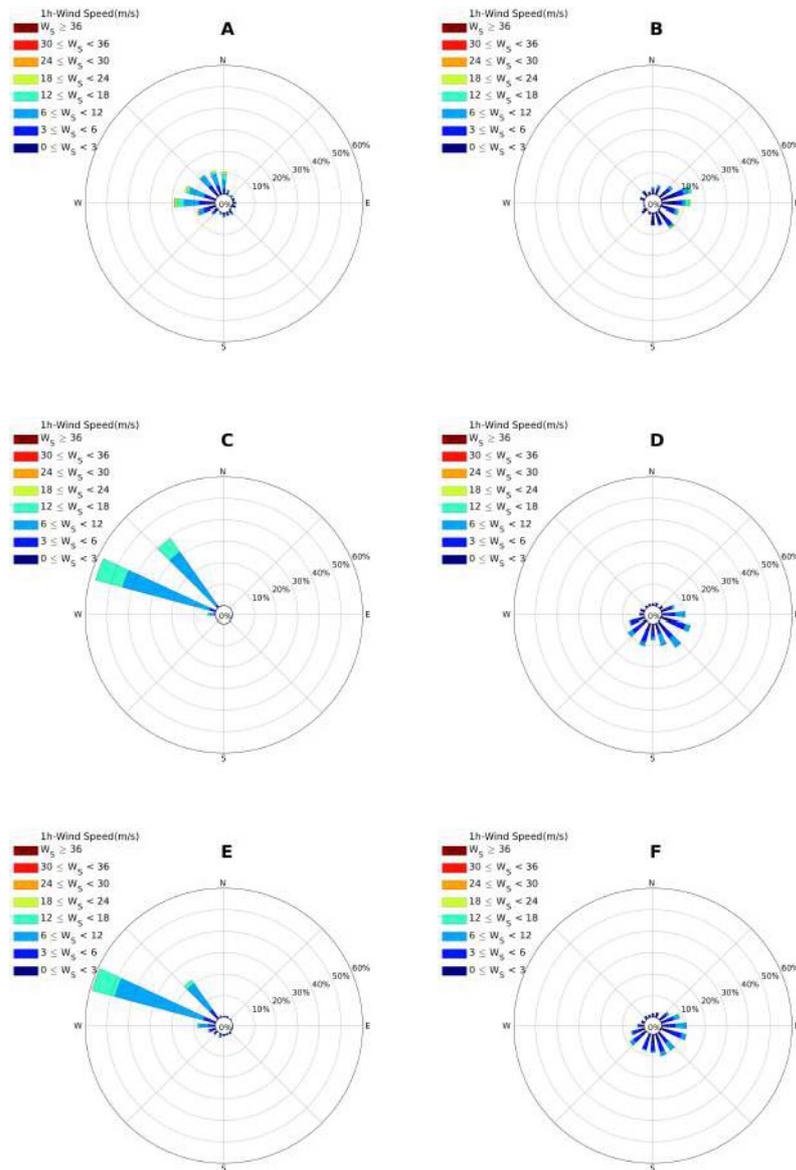
Figure 7: Hourly wind rose diagrams of observed, modeled with PBL local and non-local at January 14, 2021(panels A, C and E) and at January 09, 2021(panels B, D and F).
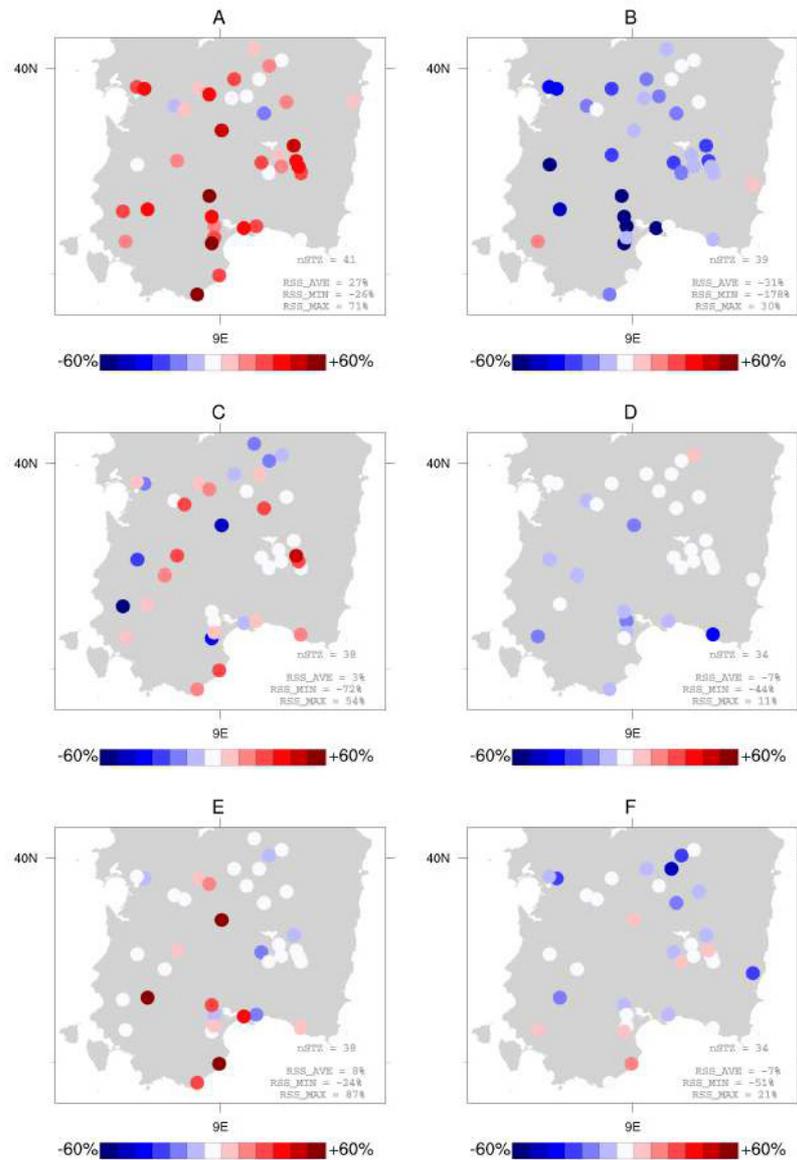
Figure 8: Daily RSST, RSSW, and RSSD at January 14, 2021(panels A, C and E) and at January 09, 2021(panels B, D and F) for each station.
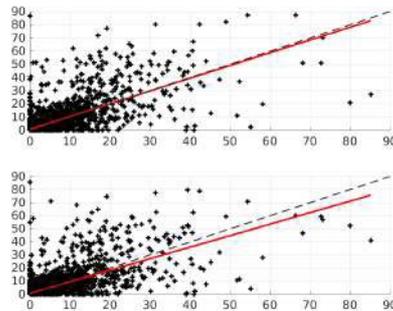
Figure 9: Scatter plot of measured (x-axis) and forecast (y-axis) daily cumulative precipitation in mm for the entire period. Top panel refers to the local scheme, bottom panel to the non-local one.
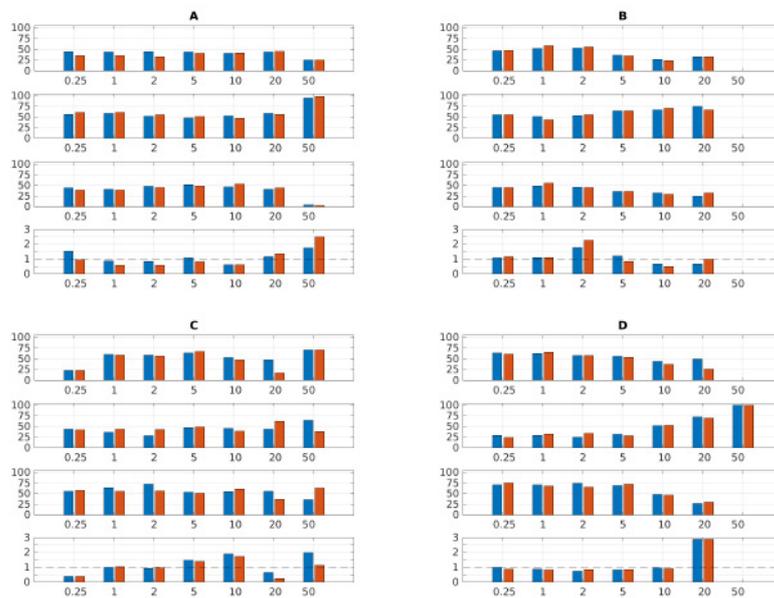
Figure 10: From the top panel: POD, FAR, SR in % and dimensionless FBI of Local(blue) and Non-local(orange) PBL scheme expressed through thresholds of 0.25, 1, 2, 5, 10, 20 and $50 mm/day$ during September(A), October(B), November(C) and December(D), 2020